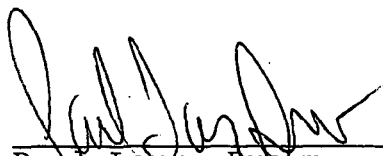


GLD2419



MICROGEOPHYSICS
CORPORATION

MCCOY, NEVADA
MICROEARTHQUAKE SURVEY



Paul Larry Brown



Robert Dorman

October 8, 1979




TABLE OF CONTENTS

	<u>PAGE</u>
1.0.0 INTRODUCTION	1
1.1.0 Microearthquake Mapping	1
1.2.0 Rock Properties	3
1.3.0 P-Wave Delay	3
1.4.0 Pseudo-Refraction	4
Introduction Bibliography	5
2.0.0 GEOLOGY AND HISTORICAL SEISMICITY	6
2.1.0 Geology of the McCoy Area	6
2.1.1 Introduction	6
2.1.2 Paleozoic and Mesozoic Geology	6
2.1.3 Cenozoic Geology	10
2.2.0 Historical Seismicity	11
Bibliography - Historical Seismicity and Geology	15
3.0.0 OPERATIONS	16
4.0.0 PSEUDO-REFRACTION SURVEY	21
4.1.0 Introduction	21
4.2.0 Data Processing Techniques	21
4.3.0 Observations	32
5.0.0 MICROEARTHQUAKES	33
5.1.0 Introduction	33
5.2.0 Observations	33
5.2.1 Detection Threshold	33
5.2.2 Methods Used in Hypocenter Locations and Velocity Model	36
5.2.3 Hypocenters	36





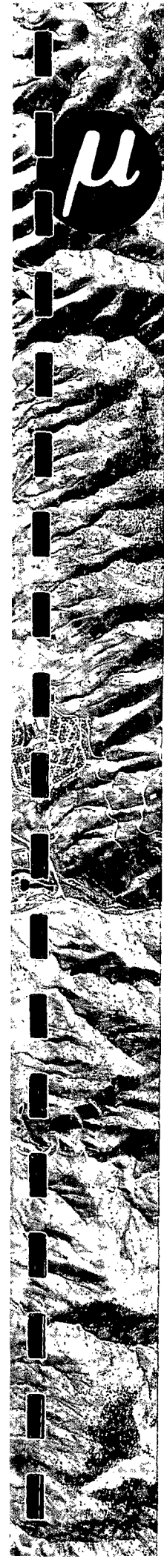
TABLE OF CONTENTS

	<u>PAGE</u>
5.2.4 Occurrence Statistics	36
5.2.5 Strain Release	44
5.2.6 First Motion Studies and Fault Plane Solutions	45
5.2.7 Poisson's Ratio	46
6.0.0 WAVE DELAY	50
6.1.0 Introduction	50
6.2.0 Data Processing Methods	50
6.3.0 Observations	54
7.0.0 COMPOSITE INTERPRETATION	55
8.0.0 SUMMARY OF CONCLUSIONS AND RECOMMENDATIONS	57
8.1.0 Conclusions	57



LIST OF FIGURES

	<u>PAGE</u>
1.0.0 INTRODUCTION	
1.1 Location and Index Map	2
2.0.0 GEOLOGY AND HISTORICAL SEISMICITY	
2.1 Geologic Map	7
2.2 Nevada Seismicity	12
2.3 Earthquake Distribution	14
2.4 Fault Plane Solutions	14
3.0.0 OPERATIONS	
3.1 Station Location and Index Map	17
3.2 Operation Schedule	20
4.0.0 PSEUDO-REFRACTION SURVEY	
4.1 Blast & Operating Station Location	22
4.2 Travel Time - Distance Curve	23
4.3 Layered Earth Model & Critical Refraction Angles	29
5.0.0 MICROEARTHQUAKES	
5.1 Hypocentral Distance vs. Magnitude and MEQ-800 System Gain	34
5.2 Detection Threshold	35
5.3 Velocity Model	37
5.4 Number of Events vs. Day of Survey	40
5.5 Number of Events vs. Hour of Day (UCT)	41
5.6 Recurrence Curve	43
5.7 Wadati Diagram	48



LIST OF FIGURES

	<u>PAGE</u>
6.0.0 WAVE DELAY	
6.1 Arrival Tims vs. Distance	52
7.0.0 COMPOSITE INTERPRETATION	
8.0.0 SUMMARY OF CONCLUSIONS AND RECOMMENDATIONS	



LIST OF TABLES

	<u>PAGE</u>
1.0.0 INTRODUCTION	
2.0.0 GEOLOGY AND HISTORICAL SEISMICITY	
3.0.0 OPERATIONS	
3.1 Station Locations and Time Corrections	18
4.0.0 PSEUDO-REFRACTION SURVEY	
4.1 Shot #1 Data	25
4.2 Shot #2 Data	26
4.3 Shot #3 Data	27
4.4 Travel Time Residuals	28
5.0.0 MICROEARTHQUAKES	
5.1 Time Corrections to Stations	38
5.2 Event Log	39
6.0.0 WAVE DELAY	
6.1 Teleseisms Recorded	51
7.0.0 COMPOSITE INTERPRETATION	
8.0.0 SUMMARY OF CONCLUSIONS AND RECOMMENDATIONS	

1.0.0 INTRODUCTION

From June 13 to July 14, 1979, MicroGeophysics Corporation conducted a passive and active seismic survey in the McCoy, Nevada area (see Figure 1.1, Location and Index Map). The seismic surveys were conducted to aid in the evaluation of the geothermal potential of the area. Passive seismic techniques employed include microearthquake mapping with measurement of acoustic rock properties and P-wave delay. The active seismic method employed was a pseudo-refraction survey of the area. Each of these methods is summarized below. A more complete discussion is contained in the Method Appendix.

1.1.0 Microearthquake Mapping

Microearthquakes are natural, discrete, seismic disturbances. These disturbances are the result of catastrophic rock failure under stress. Microearthquakes and microearthquake systems of varying activity levels have been observed at every proven geothermal area. Microearthquakes and the implied contemporaneous tectonism are a necessary ingredient for a commercial geothermal occurrence (Lange and Westphal, 1969; Ward and Bjornson, 1971; Ward and Jacob, 1971; Hamilton and Muffler, 1972; Ward, 1972; Combs and Hadley, 1977). Microearthquake activity indicates that active tectonism is currently occurring, therefore, the associated porosity and permeability are being augmented. The zone of increasing porosity and permeability can be an excellent geothermal target and may contain either the reservoir itself or the circulation path for geothermal fluids. The microearthquake

LOCATION & INDEX MAP

Drawn By: Teri Date: 9/24/79 Drawing No: McC-105 Checked By:

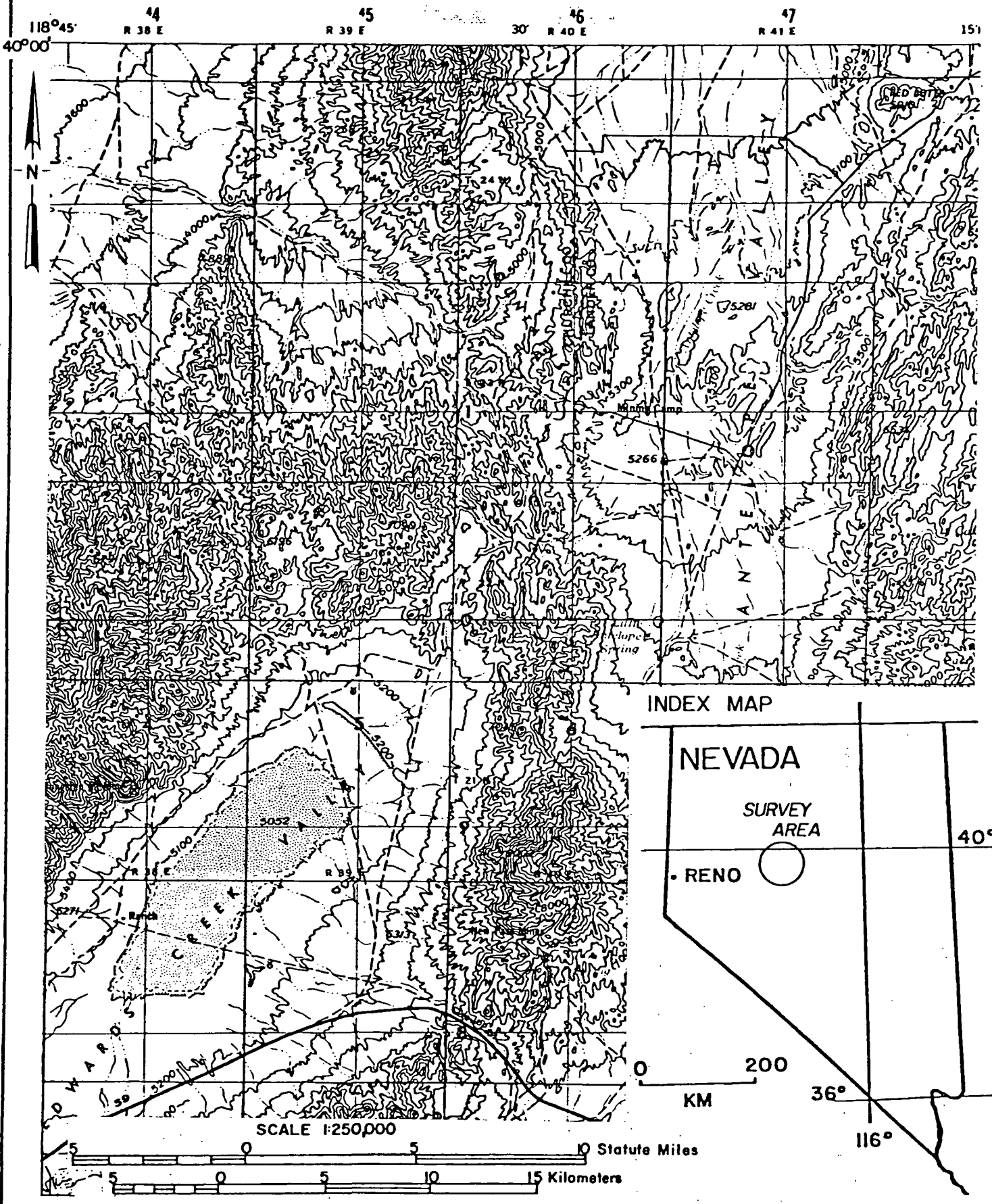



FIGURE 1.1



method does not, however, directly indicate either sufficient temperature or sufficient water recharge for a commercial system.

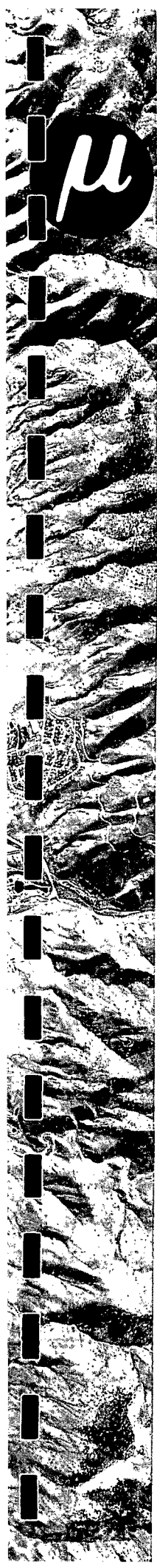
Mapping of discrete events for a geothermal area produces data for fault locations. First-motion studies produce data on the type and style of faulting and the direction of motion on faults. The statistics of occurrence of microearthquakes is used to compile a recurrence curve and to characterize and compare active geothermal areas. Strain release can be calculated, and can be interpreted in terms of total energy and fracture area associated with the microearthquakes.

1.2.0 Rock Properties

The velocity of P- and S-waves transmitted through rock is changed slightly by changes in rock temperature. Fractures in rock also change in P- and S-wave velocity in rock to some degree. If velocities are measured with a high degree of confidence, it is possible to isolate one of the requirements for a geothermal reservoir fracture porosity.

1.3.0 P-Wave Delay

When strong earthquakes occurring at large hypocentral distance are recorded, individual phase arrival times can be used to provide information about subsurface structures or to delineate areas of abnormally high temperature. Stations in the seismic array will show relative advances or delays in arrival times when the arrival times are compared to the average velocity of a chosen phase. The variations in arrival




times reflect differences in velocities near the stations caused by structural variations, lithologic variations or temperature variations. A model of subsurface velocity and an accompanying geologic model can be made to fit the observed advances and delays.

1.4.0 Pseudo-Refraction

Blasts with accurate origin times and locations can be utilized to develop a three-dimensional velocity model of the area underlying the seismic array. Blasts from different quadrants of the array will provide travel time information at different azimuths for each station. Travel times vs. radial distances to the shots can then be interpreted in terms of a three-dimensional velocity model.

This report includes sections on geology, historical seismicity, operations, pseudo-refraction, microearthquakes, associated rock properties, and P-wave delay. The final sections are a composite interpretation and a summary of conclusions from previous sections. Appendices include information about the instrumentation and methods used.

INTRODUCTION BIBLIOGRAPHY

- 
- Combs, J. and David Hadley, 1977, Microearthquake Investigation of the Mesa Geothermal Anomaly, Imperial Valley, California, *Geophysics*, Vol. 42, No. 1, pp. 17-33.
- Hamilton, R.M. and L.J.P. Muffler, 1972, Microearthquakes at the Geysers Geothermal Area, California, *JGR*, Vol. 77, No. 11, p. 2081.
- Lange, A.L., T.V. McEvilly and W.H. Westphal, 1969, Microearthquakes at the Geysers, Sonoma County, California, *JGR*, Vol. 74, p. 4377.
- Ward, P.L., 1972, Microearthquakes: Prospecting Tool and Possible Hazard in the Development of Geothermal Resources, *Geothermics*, Vol. 1, No. 1, p. 3.
- Ward, P.L. and S. Bjornson, 1971, Microearthquakes, Swarms and Geothermal Areas of Iceland, *JGR*, Vol. 76, No. 17, p. 3953.
- Ward, P.L. and R.H. Jacob, 1971, Microearthquakes: In the Ahnuachapan Geothermal Field, El Salvador, Central America, *Science*, Vol. 173, p. 328.

2.0.0 GEOLOGY AND HISTORICAL SEISMICITY

2.1.0 Geology of the McCoy Area

2.1.1 Introduction

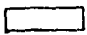



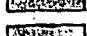
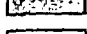
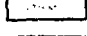
Major rock units in the McCoy, Nevada area include upper Paleozoic formations exposed in the New Pass Mountains; Mesozoic sedimentary, volcanic and intrusive rocks found at the surface or underlying much of the area; Tertiary sedimentary and volcanic rocks and Pleistocene sediments, which together cover nearly the entire surface. The area has been the site of extensive marine sedimentation during the Paleozoic and Mesozoic eras. The marine sediments have been involved in some or all of three episodes of deformation; one Permian and two Jurassic in age. During the Cretaceous period, uplift and metamorphism accompanied intrusion of granitic plutons. Continued uplift and volcanism during the Tertiary period produced great volumes of rhyolite, andesite-and basalt-tuffs, flows, and tuffaceous sediments. Normal faulting, culminating in Pleistocene time and continuing to the present, formed the "basin and range" structure and topography which characterizes the area today. Figure 2.1 shows major rock units and structure in the survey area.

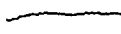



2.1.2 Paleozoic and Mesozoic Geology

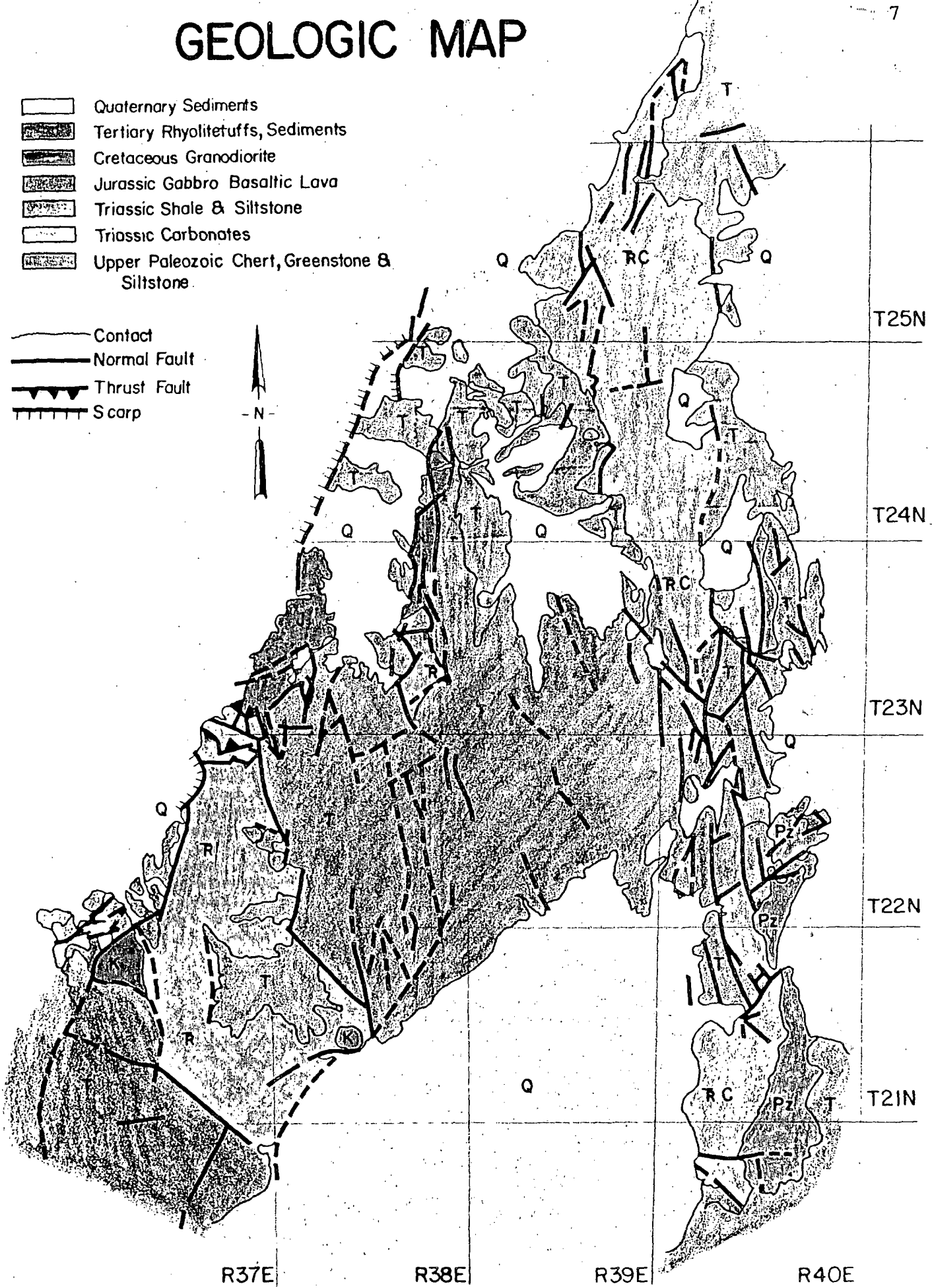
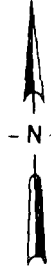
The oldest rocks found in or near the study area are late Paleozoic cherts, greenstones and siltstones. They are exposed only in the New Pass Mountains and appear to be correlative with the Pennsylvanian and Permian Havalla and Pumpnickel



GEOLOGIC MAP

-  Quaternary Sediments
-  Tertiary Rhyolite tuffs, Sediments
-  Cretaceous Granodiorite
-  Jurassic Gabbro Basaltic Lava
-  Triassic Shale & Siltstone
-  Triassic Carbonates
-  Upper Paleozoic Chert, Greenstone & Siltstone

-  Contact
-  Normal Fault
-  Thrust Fault
-  Scarp



R37E

R38E

R39E

R40E

T25N

T24N

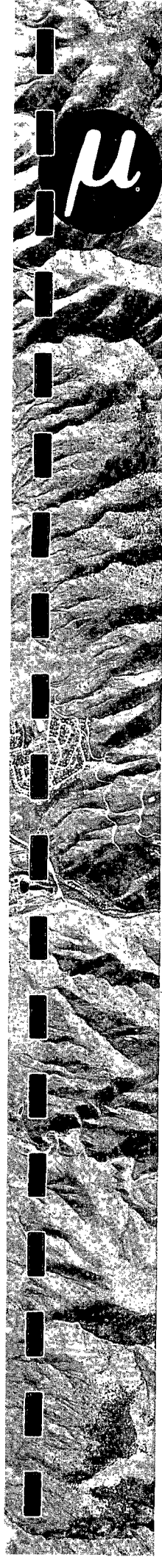
T23N

T22N

T21N

FIGURE 2.1

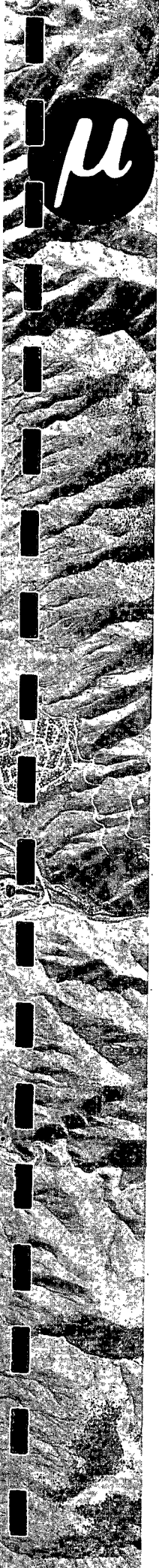
Drawn By: Teri Date: 9/7/79 Drawing No: McC-102 Checked By:



Formations described elsewhere in Nevada. Because the tectonic style of these rocks differs from that of younger, overlying formations, the upper Paleozoic rocks are thought to have been deformed in the Permian Sonoma orogeny.

Mesozoic rocks in the area include Triassic and Jurassic marine sedimentary rocks, middle Jurassic mafic intrusives and extrusives which form a lopolithic complex, and granitic intrusions of Cretaceous age. The Triassic sedimentary section varies laterally from east to west across the study area. The section begins with a thick basal chert conglomerate and continues conformably through the thin bedded limestone and siltstone of the Favret Formation, the massive limestones of the Augusta Mountain and Cane Spring Formations, and ends with the quartz sandstone (with minor limestone, shale and chert conglomerate) of the Osobb Formation.

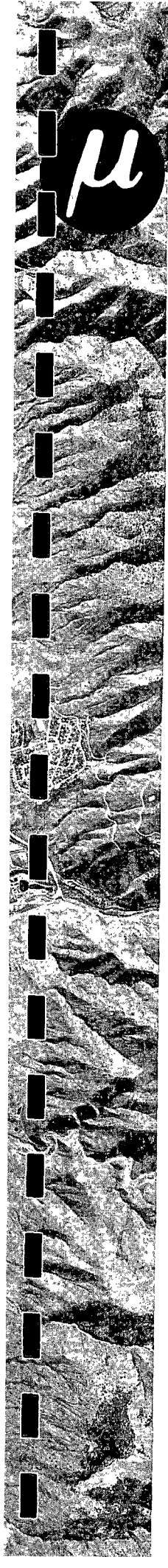
In the Clan Alpine Mountains to the west, the Triassic section is present. The section in the Clan Alpine Mountains differs slightly from equivalent rocks to the west, in that the uppermost portion contains significant carbonate plus local lenses of chert conglomerate which thin to the west, indicating a source area to the east. It is probable that the source of the conglomerates is the same as the New Pass-Augusta Mountain area conglomerate. The upper Paleozoic cherts are a likely source, and may have been exposed repeatedly throughout the Triassic period.



The contact between the eastern and western Triassic sections is not exposed. It is thought to be a thrust fault with a fairly small displacement. Facies relations suggest near shore deposition in the Clan Alpine Mountain area during late Triassic time. The area emerged in early Jurassic time and the shoreline migrated to the west where deposition continued.

During the middle Jurassic, the first of two Jurassic episodes of deformation produced broad, east-west trending isoclinal folds in the Triassic age and older rocks. At the same time, a quartz arenite was deposited, followed immediately by the extrusion of a large volume of basaltic lavas and fragmental rocks. The quartz arenite and basaltic lavas were then intruded by a body of gabbro, K/A dated at 150 myo. The gabbro is highly differentiated at its margins including the rock types picrite, olivine gabbro, hornblende gabbro and anorthosite. The intrusion of the gabbro produced thrust faults in the arenites and basalts in an anular pattern away from the intrusive center.

A second pulse of Jurassic deformation produced north-south trending folds in the entire stratigraphic section, including the gabbroic complex. Thrust faults are common throughout the Triassic and Jurassic action but displacements appear small. They may represent local slides during early phases of folding, or even soft sediment deformation during deposition.



Granitic plutons of Cretaceous age are common throughout Nevada. The two small bodies of granodiorite exposed in the Clan Alpine Mountains intrude the Triassic siltstones and shales but seem too small to have been responsible for the degree of regional metamorphism present here. For this reason, it is thought that the small granodiorite bodies may be cupolas at the top of a much larger pluton present in the area at shallow depth. Intrusion during the Cretaceous period was accompanied by regional uplift which continued throughout the Tertiary.

2.1.3 Cenozoic Geology

Tertiary and Quaternary age rocks are present at the surface over most of the study area. The oldest Tertiary rocks in the area consist of andesitic tuff breccias and basalts, K/A dated at 27 myo. These unconformably overlie Mesozoic sedimentary rocks. The northern Clan Alpine Mountains are mantled by a well layered succession of welded tuff varying in thickness from 100 to 1000 ft, with lacustrine or airfall ash interbeds. Interfingering with this are sedimentary units which have been dated as 26-21 myo.

Late Tertiary and Quaternary high angle faults are the single most common structural feature in the study area. Most trend in a northerly direction. Dip slip displacement has been the dominant movement on these faults, resulting in the typical "basin and range" topography of the area. Continuing faulting, erosion and sedimentation have filled the intervening valleys with thick units of relatively unconsolidated sediments.

2.2.0 Historical Seismicity

Seismicity in Nevada has been monitored by the Mackay School of Mines in Reno using a network of seismographs generally spread throughout the state at a 50-100 km spacing. Catalogs of the earthquakes located by this network, list events located since 1970. From 1916-1951 a two component horizontal Wiechert seismograph was in operation in Reno.

The closest seismograph to the McCoy area, operated by Mackay School of Mines, is about 50 km west, in the Stillwater Mountains. The single instrument coverage of the prospect area at that distance is not very good.

Epicenter maps from 1970-1974 show very little seismic activity in the McCoy prospect area as no large earthquakes were located there between 1916 and 1951. A definite north-south trending line of earthquakes exists south and west of the prospect area. Figure 2.2 shows the seismicity for Nevada between July 1, 1974 and December 31, 1974. This map indicates the average seismic activity in the prospect area for any given 6 month time interval between 1970 and 1974. One can see that the prospect area is located in a seismic gap on this map.

Earthquake distribution and fault mechanisms in the north-south trend of earthquakes south and west of the prospect area show a northerly trend of epicenters east of the Dixie Valley fault. At about $39^{\circ}42'N$, and $118^{\circ}5'W$ this northerly trend changes to a west-northwest trend which seems to cut across Dixie Valley.

NEVADA SEISMICITY

Drawn by Terri Dore 9/27/79 Drawing No. INC-104 Checked By:

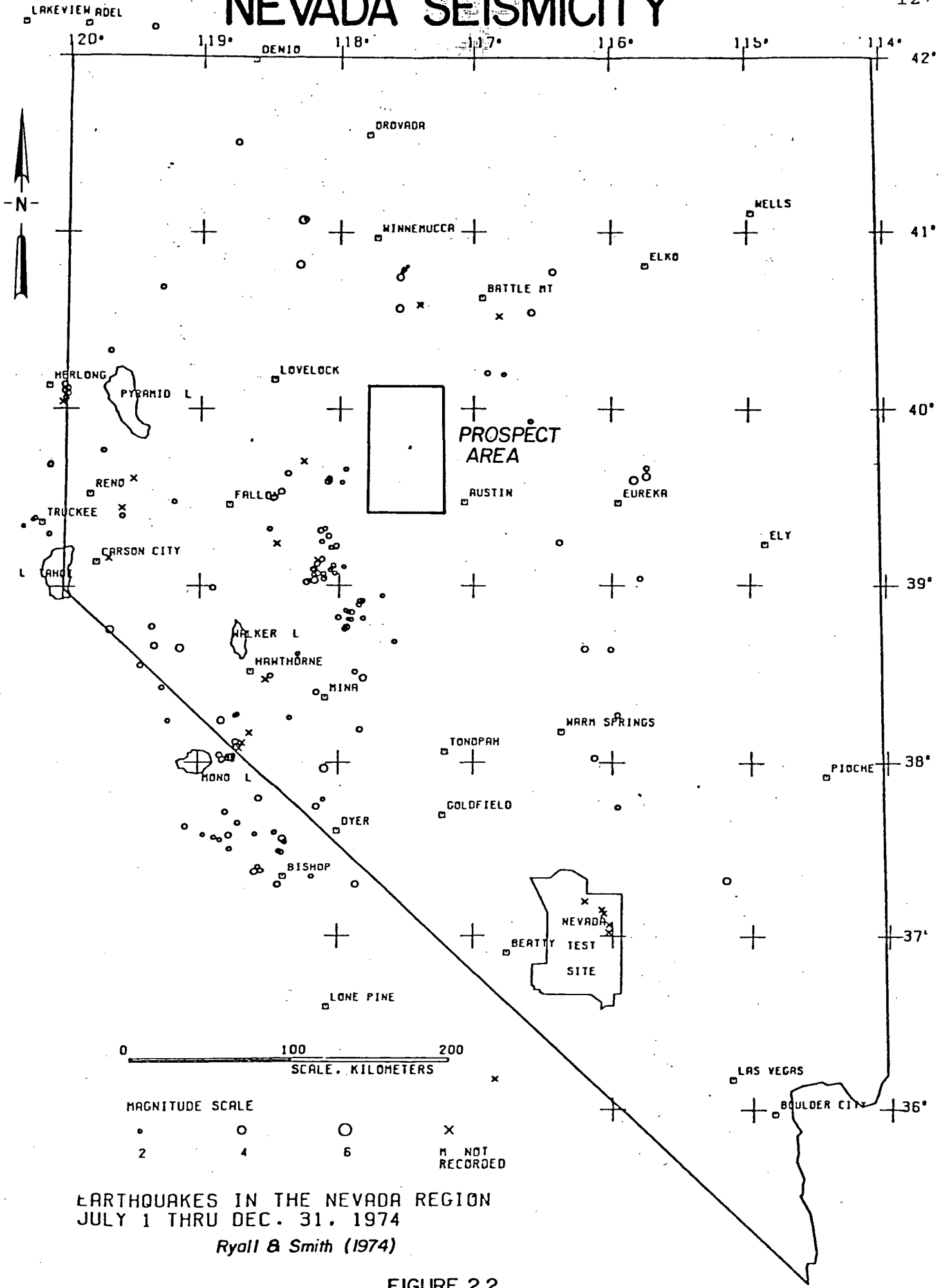
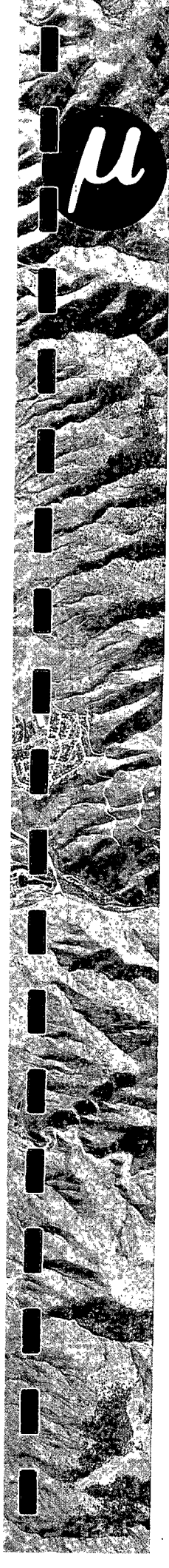


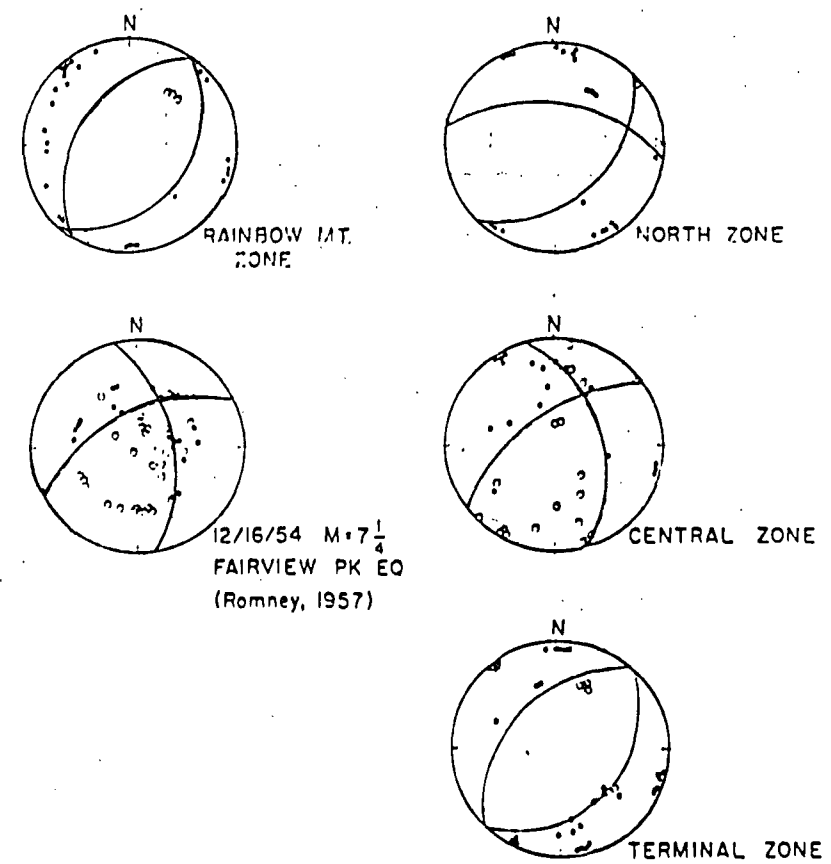
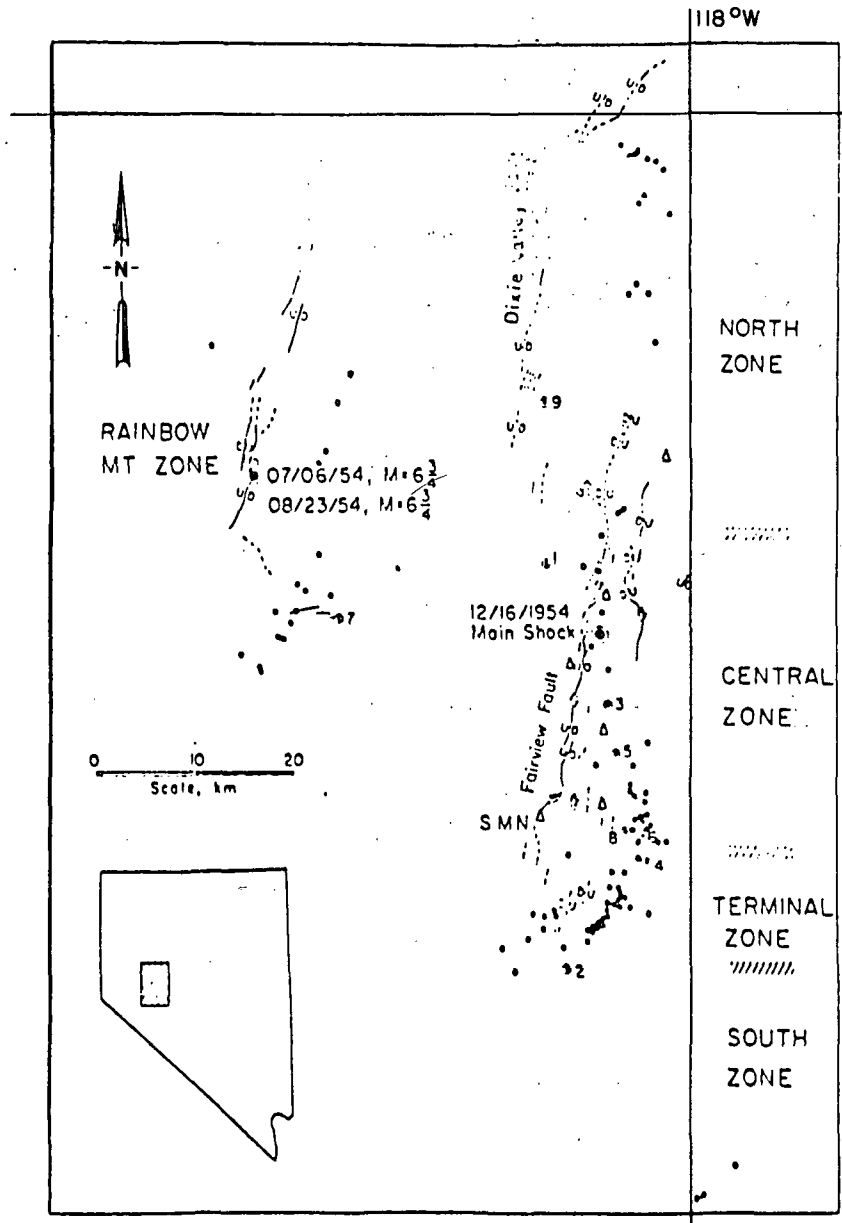
FIGURE 2.2



Fault plane solutions for both the north trending and west-northwest trending zones of hypocenters are consistent with predominantly normal faulting along fault planes oriented either northeast-southwest or east-west (Ryall and Malone, 1971). These fault planes dip southeast at about 45° and north at a steep angle respectively. Figures 2.3 and 2.4 show the earthquake distribution and fault plane solutions mentioned above. The northernmost earthquakes in Figure 2.3 are the closest historical earthquakes to the McCoy prospect area. This closest trend of earthquakes lies about 30 km southwest of the center of the McCoy survey area.

EARTHQUAKE DISTRIBUTION

FAULT PLANE SOLUTIONS



Focal mechanisms for seismic zones of this study, together with Romney's [1957] solution for the 1954 Fairview Peak earthquake. Compression first motion in P_1 or P_2 (solid circles), dilatations (open circles).

Ryall & Malone (1971)

Rainbow Mountain-Dixie Valley-Fairview Peak area, showing fault breaks mapped by Techer (1956) and Stenmons (1957), epicenters of large earthquakes in 1954 (large double circles), seismograph stations used in field studies (open triangles), earthquakes located during field studies (small double circles), and earthquakes located by analysis of data from the statewide seismic net (small closed circles).

FIGURE 2.3

FIGURE 2.4

BIBLIOGRAPHY
HISTORICAL SEISMICITY AND GEOLOGY

- Jones, Austin E., Recording of Earthquakes at Reno, 1916-1951, Bulletin of the Seismological Laboratory, Mackay School of Mines, July 1975.
- Ryall, Alan, and Stephen D. Malone, 1971, Earthquake Distribution and Mechanism of Faulting in the Rainbow Mountain-Dixie Valley-Fairview Peak Area, Central Nevada, Journal of Geophysical Research, Vol. 76, No. 2a, October 10, 1971.
- Ryall, F.D., and G.M. Smith, Earthquake Catalogs for the Period April 1, 1970 to December 31, 1974, Bulletin of the Seismological Laboratory, Mackay School of Mines.
- Stewart, John H., and John E. Carlson, Geologic Map of Nevada, 1978, USGS
- Stewart, John H., William J. Moore, and Isidore Zietz, East-West Patterns of Cenozoic Igneous Rocks, Aeromagnetic Anomalies, and Mineral Deposits, Nevada and Utah, Geological Society of America Bulletin, Vol. 88, pp. 67-77, January, 1977.
- Stewart, J.H., and E.H. McKee, 1977, Geology and Mineral Deposits of Lander County, Nevada, Part I; Geology: Nevada Bureau of Mines and Geology Bulletin 88 (pl 1, scale 1:250,000)
- Wilden, Ronald and R.C. Speed, 1974, Geology and Mineral Deposits of Churchill County, Nevada: Nevada Bureau of Mines and Geology Bulletin 93, 95 p. (pl 1, scale 1:250,000).
- Zeitz, Isidore, John H. Stewart, Francis P. Gilbert, and John R. Kirby, Aeromagnetic Map of Nevada, USGS Map MF-902.

3.0.0 OPERATIONS

A passive and active seismic survey was conducted in the McCoy, Nevada area between June 13 and July 14, 1979. Thirty-one days of recordings were obtained. Data quality was generally good with less than 10 percent loss due to wind and cultural noise.

In all, twenty-two stations were occupied during the survey. Station locations are shown in Figure 3.1. Table 3.1 lists station locations. Station placements were determined by consideration of access, array geometry, and uniform coverage of the target area.

Where a hard rock outcrop was available, the seismometer was cemented to the outcrop and covered with soil to reduce wind noise. Where hard rock was not available, the seismometer was buried from one to two feet into the soil.

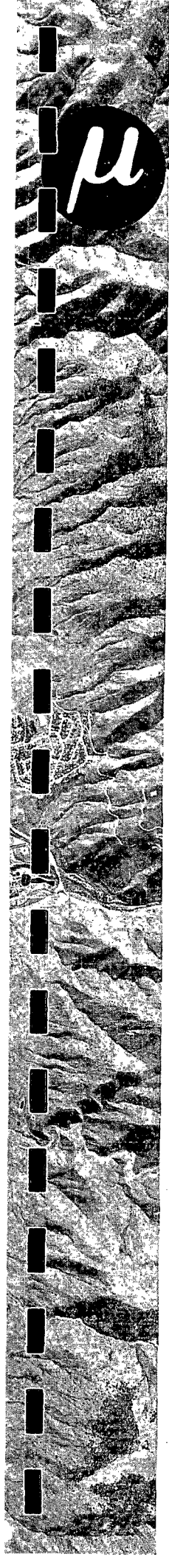
During the survey, three blasts were monitored in order to make pseudo refraction measurements. The blasts were located in abandoned mine shafts and covered with soil in order to increase maximum coupling energy. At each blast location a seismometer and MEQ-800-B seismograph recorded the origin time of the blast. All three blasts were of sufficient energy to be recorded at all stations in operation at the time of the blasts. Figure 4.1 and Plate 5.1 show station and blast locations.

Seismograph stations consisted of an L4-C vertical seismometer and an MEQ-800-B smoked paper recording system. Stations

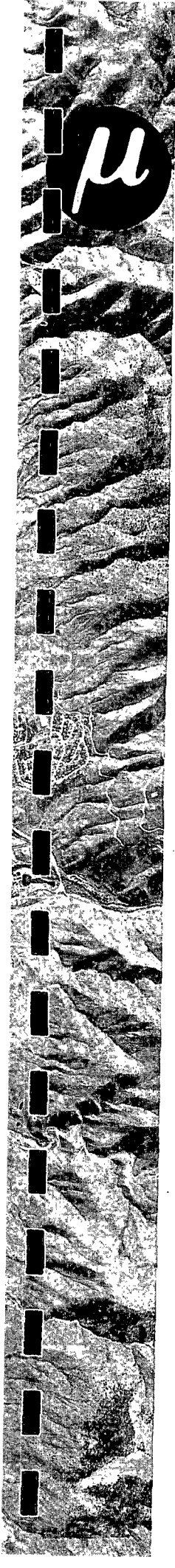
TABLE 3.1

Station Locations and Time Corrections
Origin at 39°50'N, 117°35'W, Datum 1200 m

<u>Station</u>	<u>X (km)</u>	<u>Y (km)</u>	<u>Z (km)</u>
1	-7.55	-2.55	+.290
2	-2.75	+9.54	+.070
3	-0.66	-5.52	+.665
4	-2.10	-5.00	+.685
5	+0.05	+3.71	+.210
6	+0.18	-2.08	+.836
7	+8.10	+3.82	+.379
8	-3.26	-7.74	+.487
9	-2.16	-4.19	+.701
10	-6.76	+1.09	+.272
11	-5.02	+11.02	+.039
12	+2.53	+8.11	+.171
13	+8.24	+2.12	+.385
14	+8.02	-0.75	+.517
15	+6.02	-5.00	+.563
16	-2.72	+6.69	+.100
17	+3.55	+2.83	+.254
18	+4.52	-3.33	+.487
19	+4.36	+0.41	+.333
20	+4.36	-7.24	+.563
21	+9.10	-4.90	+.548
22	+7.12	+8.05	+.324



1, 2, 3, 5, 6, and 8 were telemetered to a central location at station 9. Details of the equipment used are contained in the instrumentation appendix. Figure 3.2 is a detailed operations schedule for all stations.



1, 2, 3, 5, 6, and 8 were telemetered to a central location at station 9. Details of the equipment used are contained in the instrumentation appendix. Figure 3.2 is a detailed operations schedule for all stations.

OPERATION SCHEDULE

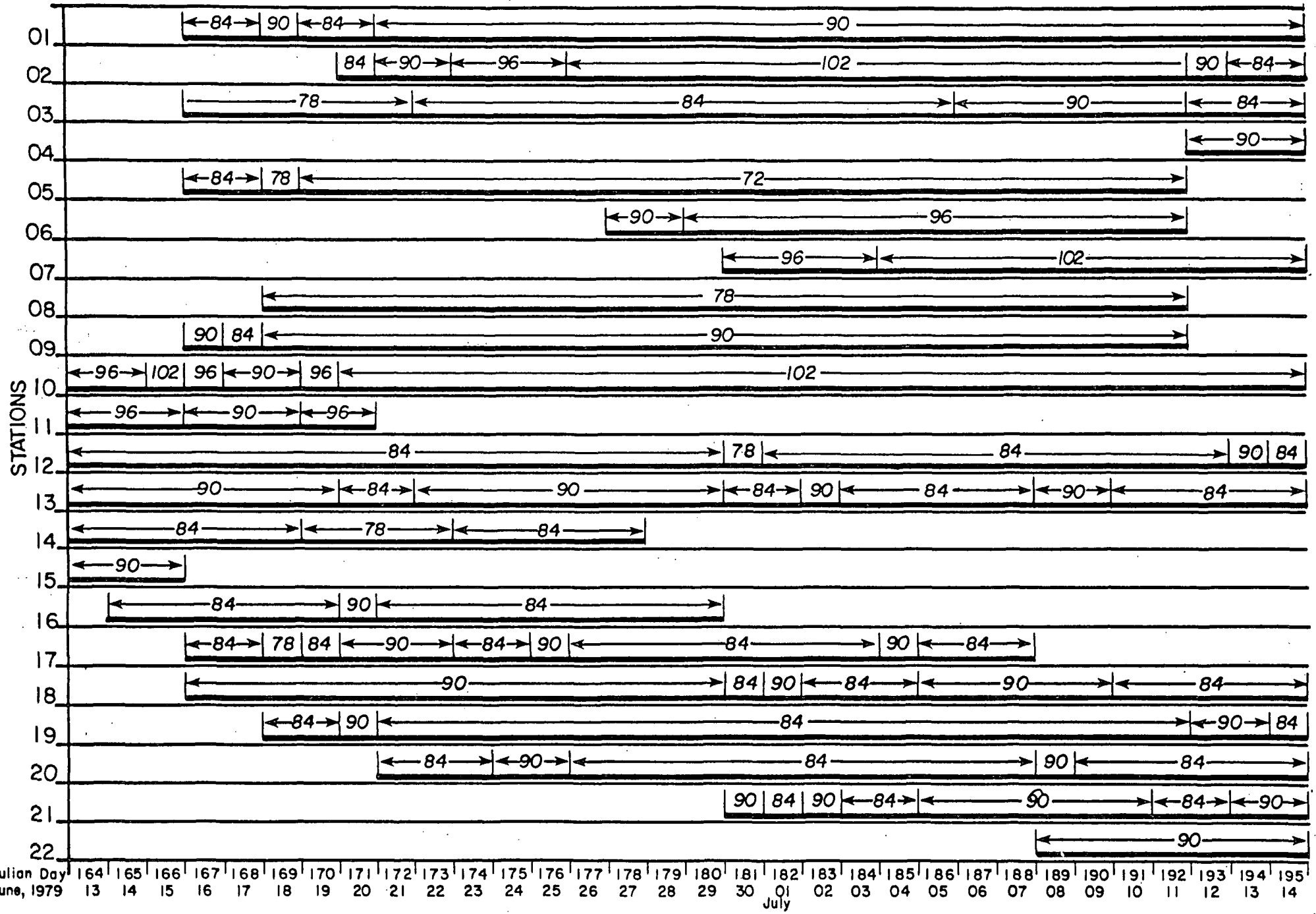


FIGURE 3.2

4.0.0 PSEUDO-REFRACTION SURVEY

4.1.0 Introduction

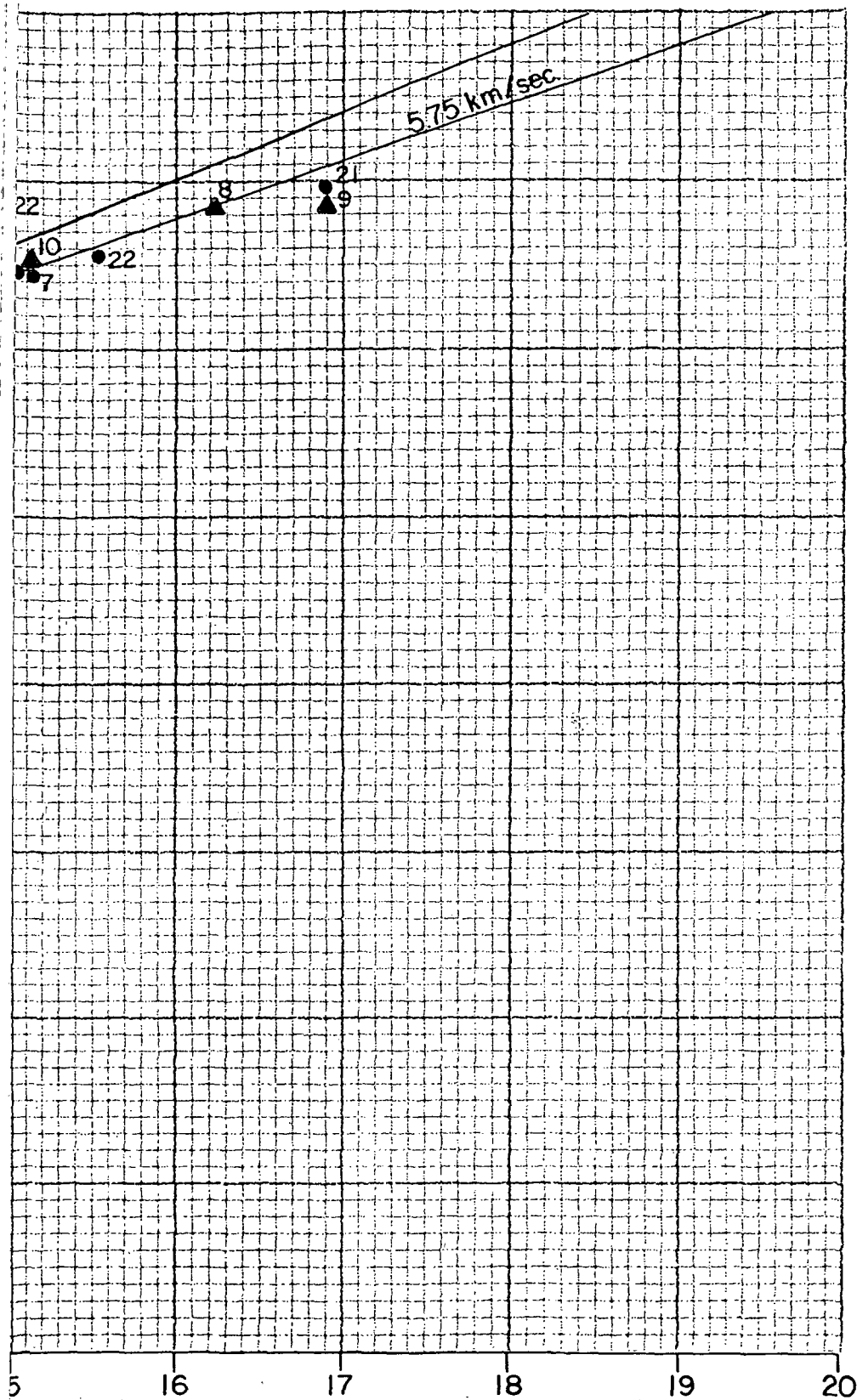
This section of the report describes the pseudo-refraction survey conducted in the McCoy area. Three blasts are used to determine the velocity structure underlying the survey area. The blast locations and stations which are operating at the time of these shots are shown in Figure 4.1. This section includes discussions on data processing techniques for pseudo-refraction and observations obtained from the pseudo refraction survey.

4.2.0 Data Processing Techniques

P- and S-wave arrivals from the blasts were picked off from smoked paper records at each station. The shot origin time was picked from a seismograph record obtained at the blast site. Travel times to each station were determined for each blast and plotted vs. radial distance to the station. The points obtained in the travel time-distance plot can be fit with straight line segments which have slopes and time axis intercepts representing the inverse velocities in the depths to different refractors in a layered earth model. Figure 4.2 shows the composite travel time-distance curve for all three shots at McCoy.

Once a first approximation of a layered earth model is made using the composite travel time-distance curve, computer processing is used to refine the model. The computer program is a refraction forward modeling routine. The user must input

TRAVEL TIME - DISTANCE CURVE




BLAST NO. 1 ●
BLAST NO. 2 ▲
BLAST NO. 3 x

LAYERED EARTH
4.0 1.0
5.0 3.0
5.75

Drawn By: Teri Date: 9/25/79 Drawing No: MC-C-109 Checked By:

FIGURE 4.2



a desired velocity model, actual travel times and distances for each receiving station. Initially, all travel times are corrected to a datum by subtracting time from each station based on a uniform first layer velocity. After the initial corrections, the travel times at each station are changed to reflect the actual velocity of the first layer under each station. Tables 4.1, 4.2 and 4.3 show the station distances, raw travel times, velocities of first layers, elevation corrections and final corrected travel times for each blast. The elevation corrections were made along a downward vertical path rather than along an average inclination angle.

The corrected travel times listed in Tables 4.1, 4.2 and 4.3 are then input into the computer program to obtain a finalized best fit to a layered earth model. Residuals from this best fitting layered earth model can then be analyzed.

Table 4.4 lists stations and their time residuals from a best fitting layered earth model. The best fitting model used is shown in Figure 4.3, along with raypaths to each refractor. Time residuals at each station are accounted for by replacement of material of one velocity with material of another velocity under the station. This solution is necessarily indeterminate unless the velocities used for each material are fixed. In this case, the velocities are fixed to the 4.0 km/sec, 5.0 km/sec and 5.75 km/sec values obtained for the layered earth model. Using these velocities travel times through 100 meters of each material are:

TABLE 4.1
Shot #1 Data

Shot Locations:	X(km)	Y(km)	Z(km)	Time(Day, Hr:Min:Sec)
Origin:	-6.76	+1.09	+0.272	189,06:37:03.73

Station	Radial Distance (km)	Raw Travel Time (sec)	Velocity of Surface Layer (km/sec)	Corrected Travel Time (sec)
1	3.75	1.09	5	.98
9	7.00	1.59	5	1.40
5	7.35	2.02	4	1.91
6	7.64	2.12	4	1.91
3	9.00	1.96	5	1.77
2	9.33	2.24	4	2.17
19	11.17	2.65	4	2.51
12	11.62	2.77	4	2.67
18	12.13	2.82	5	2.67
20	13.92	2.98	5	2.81
13	15.06	3.39	4	3.24
7	15.12	3.37	4	3.22
22	15.57	3.42	4	3.28
21	16.90	3.64	5	3.48

TABLE 4.2
Shot #2 Data

Shot Locations:	X (km)	Y (km)	Z (km)	Time (Day, Hr:Min:Sec)
Origin:	+8.10	+3.82	+3.79	190,05:48:4.70
Station	Radial Distance (km)	Raw Travel Time (sec)	Velocity of Surface Layer (km/sec)	Corrected Travel Time (sec)
19	5.06	1.18	5	1.07
12	7.01	1.57	4	1.48
18	8.01	1.83	5	1.69
5	8.06	2.17	4	2.07
21	8.78	2.17	5	2.01
6	9.91	2.50	4	2.29
20	11.70	2.52	5	2.36
3	12.82	2.85	5	2.67
9	13.05	2.88	5	2.69
10	15.12	3.37	5	3.27
8	16.22	3.59	4	3.45
1	16.90	3.55	5	3.44

TABLE 4.3
Shot #3 Data

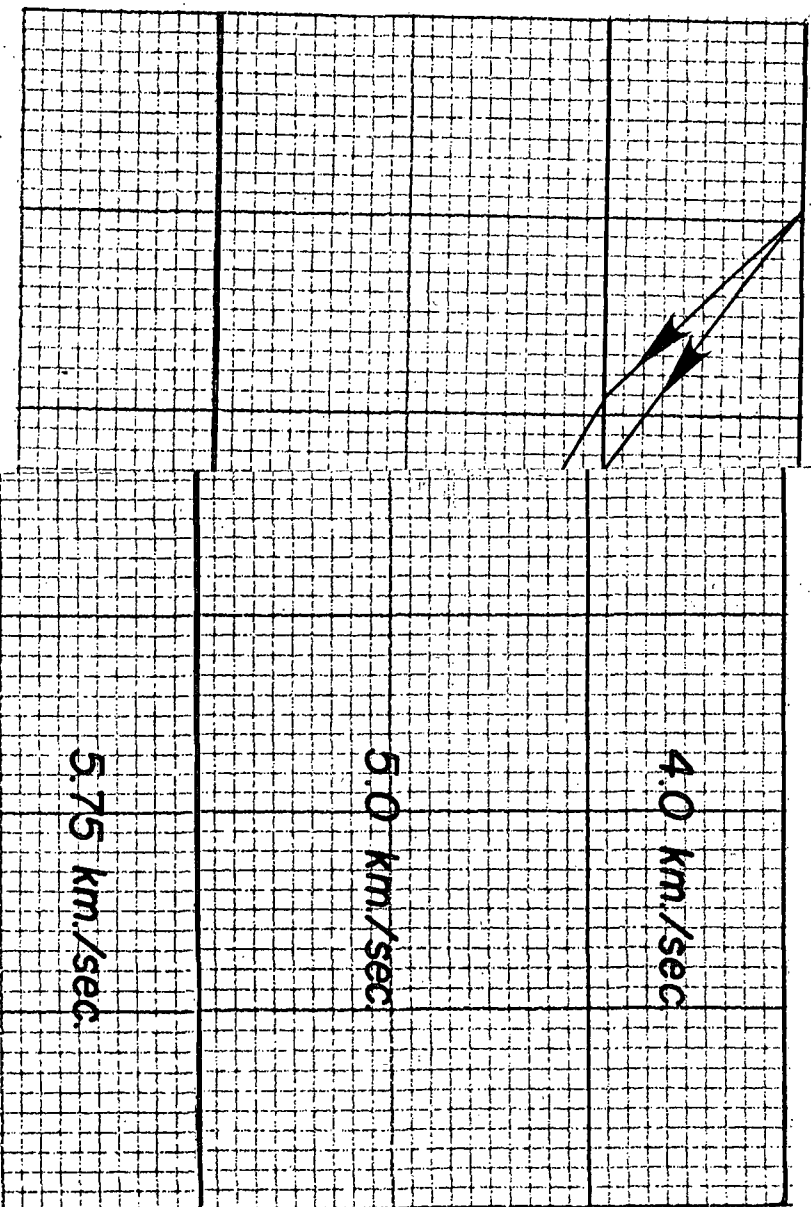
Shot Locations:				
	X (km)	Y (km)	Z (km)	Time (Day, Hr:Min:Sec)
Origin:	-2.10	-5.00	+ .685	194,14:24:03.33
Station	Radial Distance (km)	Raw Travel Time (sec)	Velocity of Surface Layer (km/sec)	Corrected Travel Time (sec)
1	6.00	1.40	5	1.20
18	6.87	1.84	5	1.61
20	6.85	1.79	5	1.54
10	7.70	1.72	5	1.53
19	8.43	2.23	4	2.01
21	11.20	2.62	5	2.37
13	12.60	2.94	4	2.71
7	13.50	3.06	4	2.83
12	13.88	3.26	4	3.08
2	14.56	3.48	4	3.33
22	15.93	3.80	4	3.48

TABLE 4.4
Travel Time Residuals

- is early arrival + is late arrival

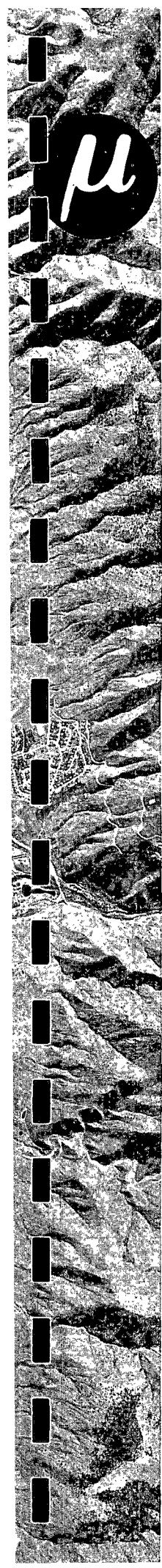
Shot #1		Shot #2		Shot #3	
Station	Residual (ms)	Station	Residual (ms)	Station	Residual (ms)
2	+10	1	-110	1	-300
3	-280	3	-170	2	+100
5	+70	5	+90	7	-120
6	-10	6	0	10	-310
7	-100	8	0	12	0
9	-280	9	-180	13	-80
12	+50	10	+30	18	-80
13	-60	12	-220	19	+10
18	-50	18	-210	20	-140
19	-30	19	-250	21	-180
20	-210	20	-290	22	+70
21	-200	21	-50		
22	-150				

Drawn By: Teri Date: 9/26/79 Drawing No: McC-110 Checked By:



RED EARTH MODEL 8 REFRACTION ANGLES

FIGURE 4.3



25 milliseconds at 4.0 km/sec

20 milliseconds at 5.0 km/sec

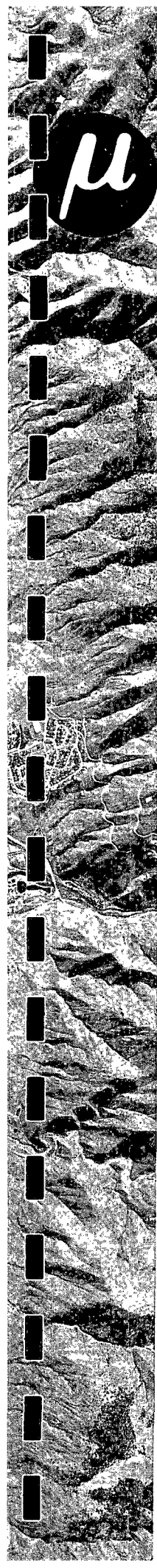
17 milliseconds at 5.75 km/sec

Thus interchanging 4.0 km/sec and 5.0 km/sec material gives a 5 ms travel time change per 100 meters of interchanged material and interchange of 5.0 km/sec and 5.75 km/sec material gives a 3 ms travel time change per 100 meters of interchanged material. These values of 5 ms/100 meters and 3 ms/100 meters are corrected for the average refraction angles shown in Figure 4.3. The corrected values become 9 ms/100 meters of 4.0 km/sec and 5.0 km/sec interchange and 6 ms/100 meters of 5.0 km/sec and 5.75 km/sec interchange. Thus, one must add enough faster material at a station to account for an early arrival (negative travel time residual) or add enough slower material at a station to account for a late arrival (positive travel time residual). Deviations from the layered earth model under each shot point also must be accounted for. Thus the total travel time residual must be accounted for by material replacement both at the shot and receiving station. This is best accomplished by shifting the time residuals at each receiving station for each shot based on the velocity structure under each shot point. The shifts used in this survey were:

Shot #1 + 90 ms

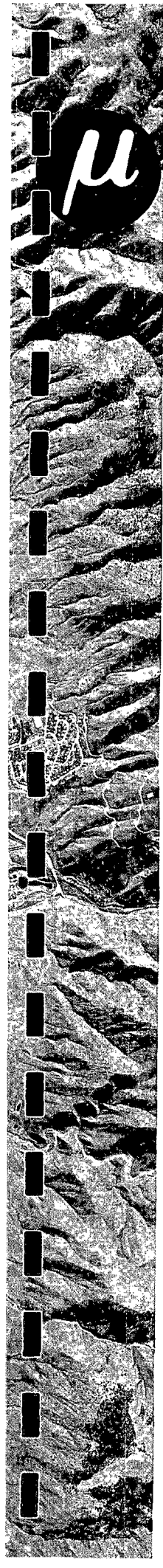
Shot #2 + 70 ms

Shot #3 + 90 ms



All three shot points are located where 5.0 km/sec material is at or very near the surface. Thus this high velocity material would account for part of an early arrival at a receiving station. Also, a late arrival at a receiving station has to be made even later to compensate high velocity material at the shot point.

The travel time residual at the station (after shifting to account for the material present at the shot point) is then accounted for by moving the 5.0 km/sec layer up or down. The 5.0 km/sec layer is moved up to account for negative travel time residuals (early arrivals) and moved down to account for positive travel time residuals (late arrivals). The resultant depth to the 5 km/sec layer is then plotted on a map at the point where the seismic raypath traveling at the critical refraction angle intersects the 5.0 km/sec layer. If the 5.0 km/sec layer is moved to the surface, and there is still a resultant travel time residual, the resultant travel time residual is accounted for by moving the 5.75 km/sec layer up at a rate of 100 meters/6 milliseconds. When the 5.0 km/sec layer is moved down to account for positive travel time residuals (late arrival at the receiving station), the travel time residual is accounted for totally by changing the depth of this 5 km/sec layer, under the assumption that the 5.75 km/sec layer is too deep to actually be the refractor on which the seismic ray travels to the receiving section.



The depths to each layer which have been plotted on the map are then contoured to show the resulting three-dimensional velocity model.

4.3.0 Observations

Plate 4.1 shows the contour map of depth to the 5 km/sec layer. It can be seen that the 5.0 km/sec layer is at the surface in the southwest and east-central sections of the survey area. These areas are highlighted with vertical lines on Plate 4.1. The 5.0 km/sec layer drops off steeply to the north, east, and west respectively of these highs. The maximum depth, near station 5 in the central part of the array, is about 3.5 km. Areas where the 5.0 km/sec layer is deeper than 2 km are highlighted in a dotted pattern on Plate 4.1. These steep gradients may represent faulting with a considerable amount of dip-slip displacement.

5.0.0 MICROEARTHQUAKES

5.1.0 Introduction

This section of the report concerns the local microearthquakes detected during the seismic survey of the McCoy, Nevada area. Seismic activity is low, with 36 microearthquakes being recorded during the 31 record days. An event is designated a local microearthquake if it shows a seismic signature with an S-P time of 5 seconds or less on at least one station. Of the 36 microearthquakes recorded, 30 were located. Included in this section are discussions of the detection threshold, methods used in hypocenter location and the velocity model used, hypocenters, earthquake occurrence statistics, estimated strain release, first motion studies, and Poisson's Ratio.

5.2.0 Observations

5.2.1 Detection Threshold

The detection threshold distance is defined as the largest hypocentral distance at which an earthquake of a given magnitude will produce a trace displacement of at least 2 mm on the detecting instrument. Therefore, any event within the detection-threshold distance would be detected on at least one station if the event exceeds the magnitude for which the detection-threshold is calculated. Detection-threshold contour maps are derived from the trace amplitude versus distance relationship for various magnitudes, considering the station gain and signal-to-noise ratio. A graph of Hypocentral Distance vs. Magnitude and MEQ-800 system gain is shown in Figure 5.1. The detection-threshold contour map as calculated from a magnitude of 0.0 is depicted on Figure 5.2. From this contour map, it can be stated that for areas within 3 km of the array the detection-threshold approached a magnitude of -0.5.

LOW = 5Hz HIGH = 30 Hz
 DISPLACEMENT GAIN AT 20 HERTZ (10^6)

0.08 0.16 0.33 0.65 1.30 2.60 3.20

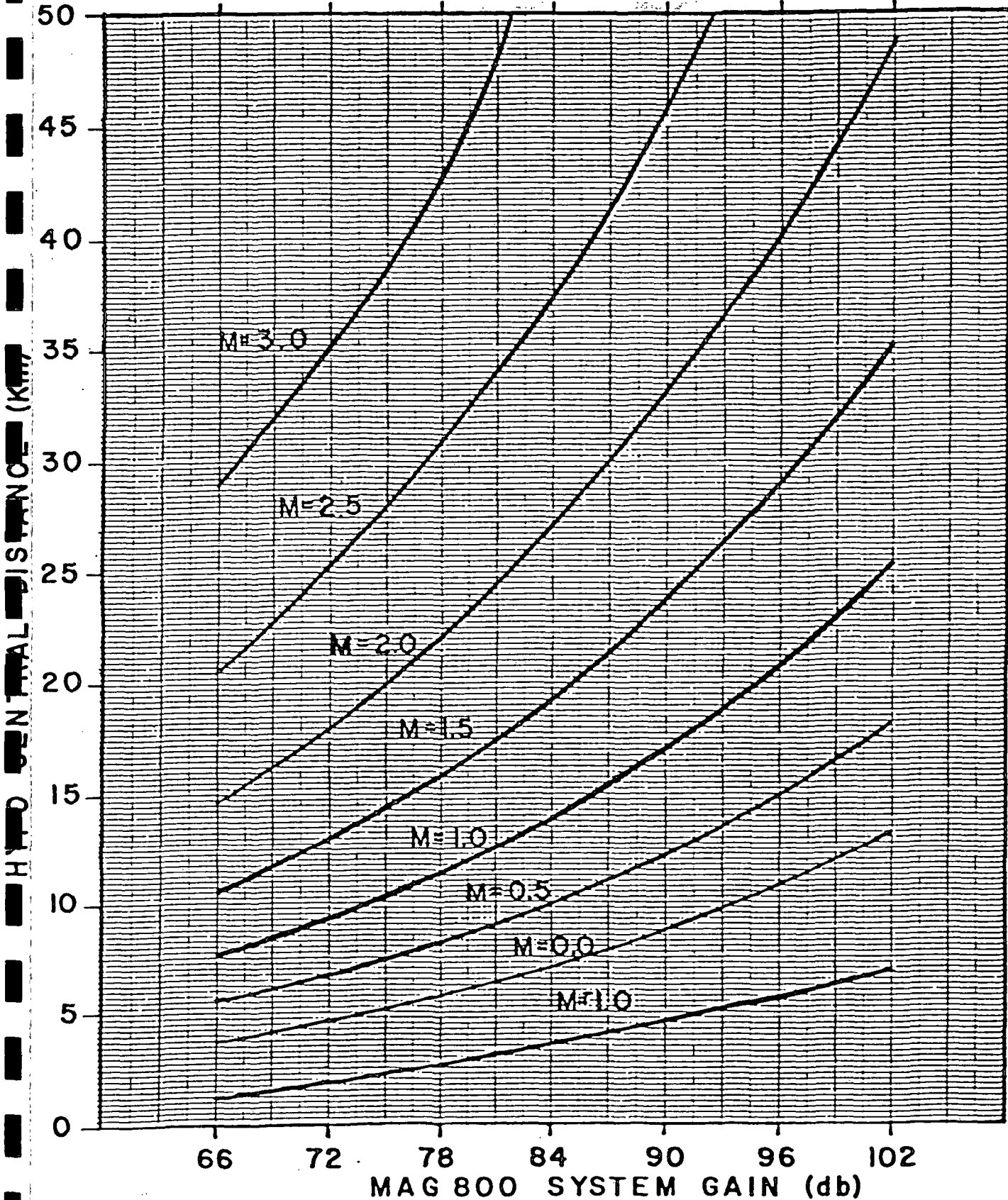
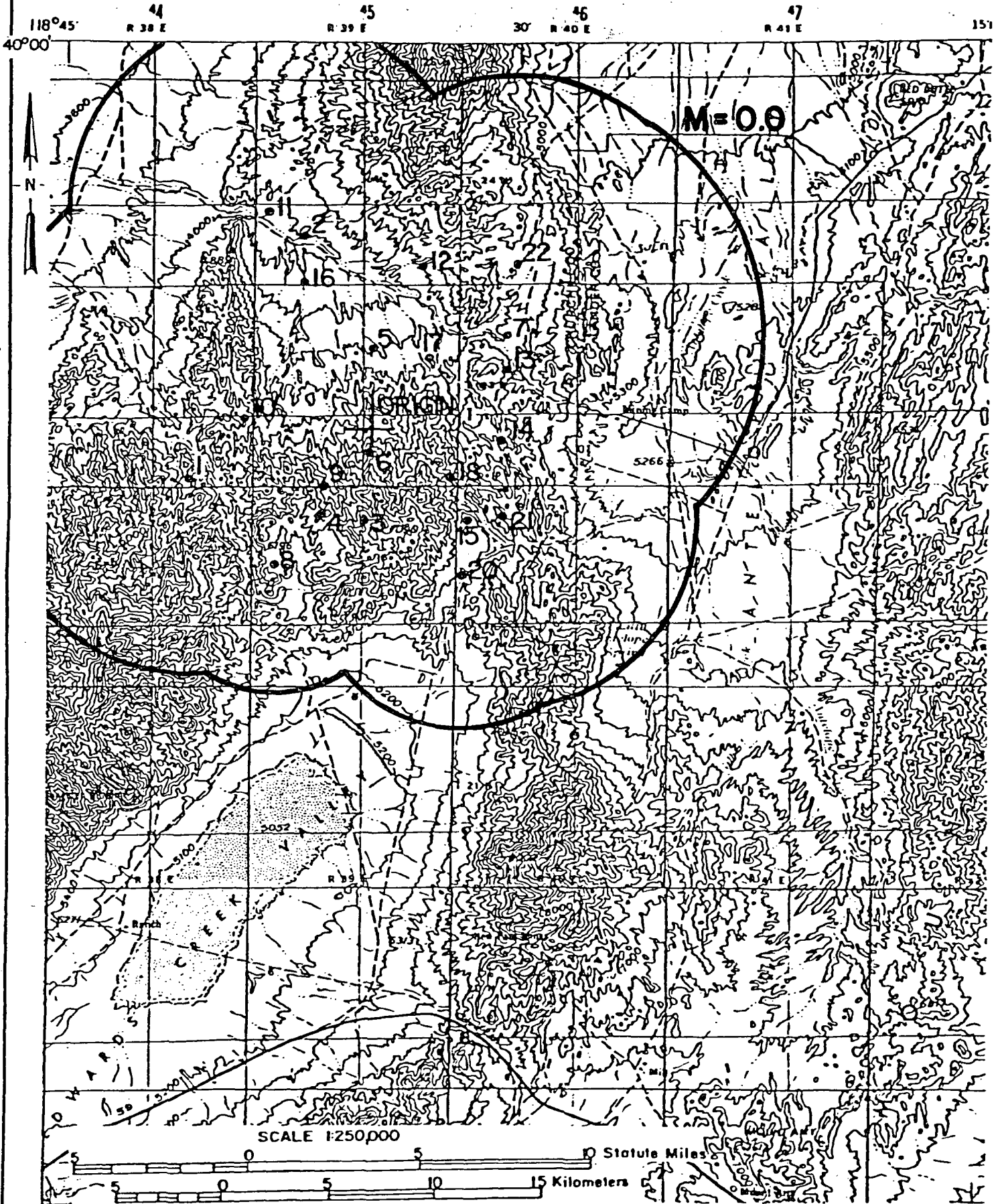


FIGURE 5.1

DETECTION THRESHOLD



Drawn By: Teri Date: 9/24/79 Drawing No: MCC-112 Checked By:

FIGURE 5.2

5.2.2 Methods Used in Hypocenter Locations and Velocity Model

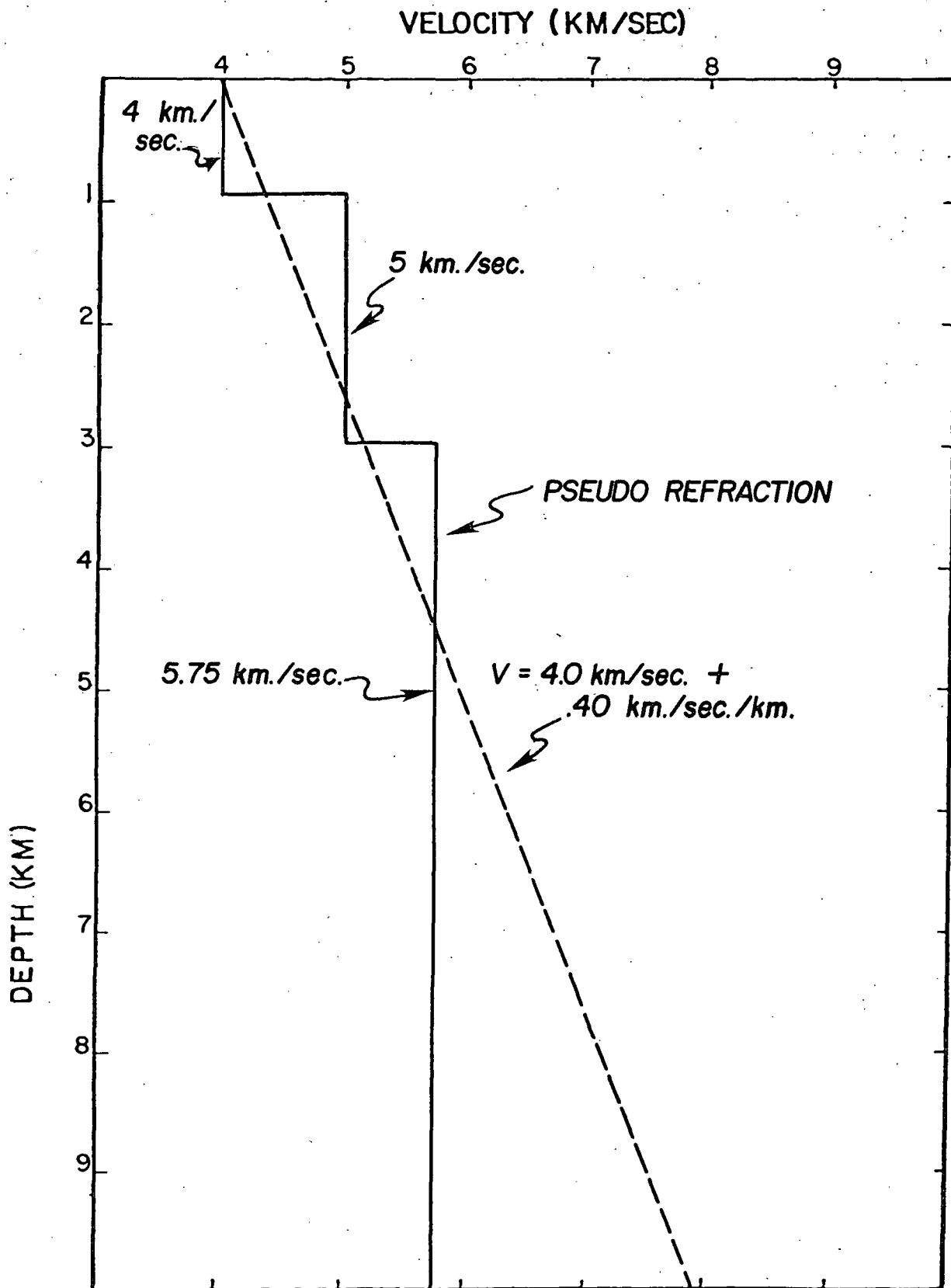
Earthquakes showing good P arrivals at 3 or more stations are located using a linear increase with depth velocity model. The velocity model chosen has a surface velocity of 4.0 km/sec and an acceleration with depth of .40 km/sec/km. This velocity model produces a good fit to the layered earth model found in the pseudo-refraction survey. The layered earth model and the linear increase with depth model are shown in Figure 5.3. Time advances and delays are added to each station based on the travel time residuals from the pseudo-refraction survey. Table 5.1 lists these advances and delays. The three shots used in the pseudo refraction survey are then located using the linear increase with depth velocity model. Station advances and delays are adjusted until the computed locations of the shots agree with the actual locations within 1 km in epicenter. There is less control on the depth. Depth errors in show locations are 3.7 km, 0 km, and 1.6 km for shots 1, 2, and 3 respectively.

5.2.3 Hypocenters

Plate 5.1 shows hypocenters of the located earthquakes. Table 5.2 lists all of these located earthquakes. All locations are in km based on a cartesian coordinate system with the origin at 39°50' north and 117°35' west. The datum is the same as used in the pseudo refraction survey, 1200 meters above sea level.

5.2.4 Occurrence Statistics

Figures 5.4 and 5.5 are plots of the number of earthquakes versus time of occurrence. Figure 5.4 plots the number of



VELOCITY MODEL

FIGURE 5.3

TABLE 5.1
TIME CORRECTIONS TO STATIONS

STATION	CORRECTION (ms)	STATION	CORRECTION (ms)
1	+ 100	11	0
2	- 100	12	0
3	+ 250	13	0
4	+ 250	14	0
5	-100	15	0
6	- 100	16	- 100
7	0	17	0
8	+ 100	18	0
9	+ 250	19	- 100
10	+ 250	20	+ 100
		21	+ 100
		22	0

+ ms is delay

- ms is advance

TABLE 5.2
EVENT LOG

DAY	HR	MIN	SEC	X	Y	Z	MAG
169	04	13	14.65	10.4	-12.4	3.5	1.5
169	06	40	11.82	4.4	10.5	3.9	-0.1
169	11	03	29.13	17.3	4.0	3.2	1.1
171	08	49	21.18	18.8	3.6	1.8	0.9
171	18	01	54.53	-5.7	5.0	8.8	0.7
171	18	02	40.61	-4.4	4.3	6.0	0.5
172	12	28	5.00	-32.0	-15.8	7.7	2.8
172	12	34	15.53	-32.5	-13.7	2.9	2.6
172	12	34	23.97	-31.5	-15.3	3.6	2.9
172	15	09	32.98	-30.8	-13.6	4.2	2.1
172	15	15	33.39	-32.5	-14.6	3.8	1.9
172	15	21	42.99	-30.1	-15.0	3.3	2.2
172	16	50	40.17	-27.5	-11.1	8.6	3.1
174	04	11	11.77	9.0	14.6	3.3	1.1
175	04	22	16.62	-1.6	-5.6	5.2	-0.9
175	23	46	48.40	5.9	4.8	7.8	0.9
176	01	02	32.57	5.8	4.9	7.8	-0.1
176	02	24	36.85	-3.8	6.3	9.3	0.5
176	09	18	7.18	2.0	-23.6	4.4	1.8
176	19	16	23.58	10.0	-7.3	3.7	0.9
177	12	57	53.10	-0.7	17.0	6.1	0.6
182	18	54	9.55	-7.8	-4.9	4.8	-0.1
184	01	07	3.16	3.0	-11.0	5.4	0.4
186	07	15	39.12	8.3	2.6	6.9	0.2
189	02	17	33.09	3.6	-12.0	5.4	0.4
189	04	02	8.44	20.3	17.8	4.2	1.7
189	07	23	49.53	3.3	-10.9	4.2	-0.3
190	03	07	58.49	-20.7	6.2	8.2	1.6
192	06	19	29.05	-15.9	2.6	4.5	0.2
192	16	16	46.05	-12.6	1.4	4.2	1.0

NUMBER OF EVENTS VS. DAY OF SURVEY

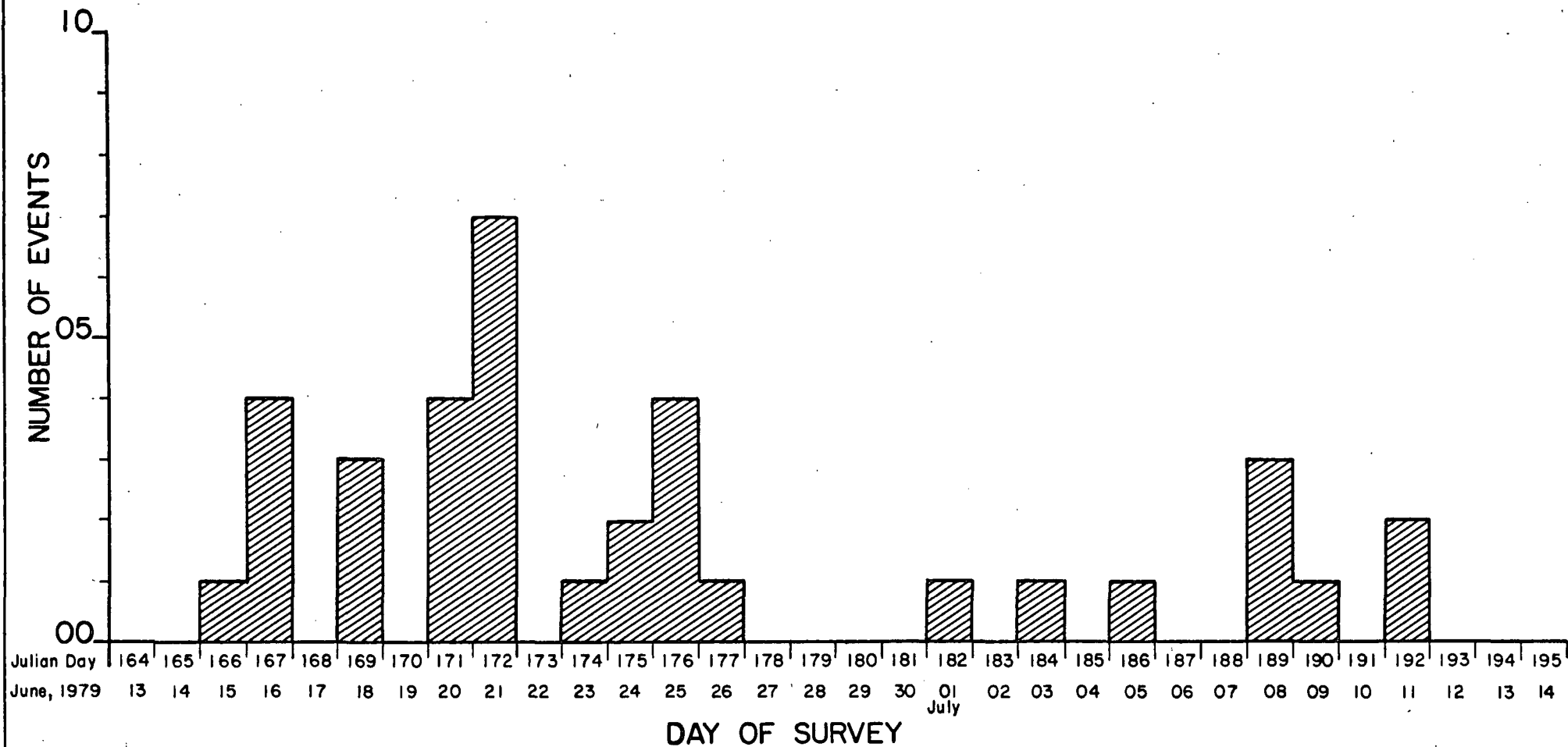


FIGURE 5.4

NUMBER OF EVENTS VS. HOUR OF DAY (UCT)

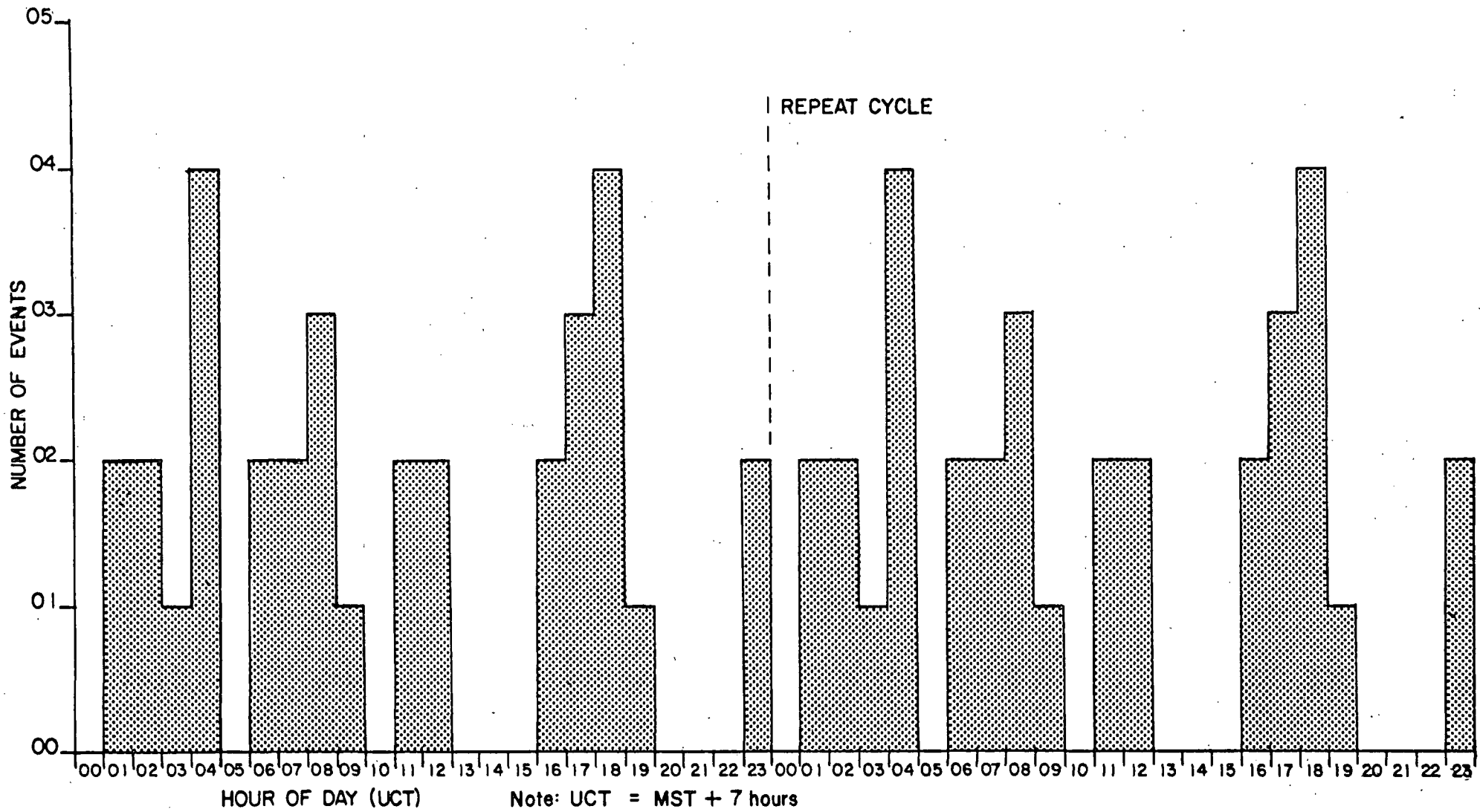
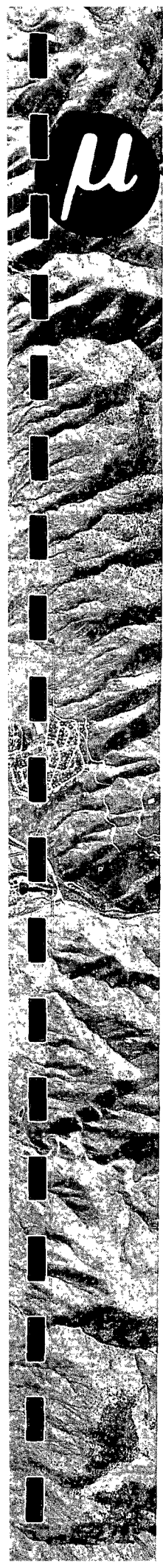


FIGURE 5.5



earthquakes versus the day of the survey. Figure 5.5 plots earthquake occurrence versus the hour for all days of the survey. All earthquakes recorded (located and unlocated) are shown in these figures. As can be seen in Figure 5.4, there are no large swarms of earthquakes during the survey. The largest concentration of earthquake activity occurs on day 172 (June 21). The small swarm on day 172 reflects distant local earthquake activity occurring southwest of the seismograph array along the eastern side of Dixie Valley. The distribution of events by hour (Figure 5.5) shows a fairly diffuse pattern. The McCoy survey area is quite remote and thus there is little cultural noise present during the day hours to obscure the seismograph records. Thus there is no grouping of events during night hours as is commonly seen in more noisy areas.

A characteristic of seismicity is the recurrence curve. The recurrence curve is a plot of the earthquake magnitude vs the log of the cumulative number of earthquakes. This plot is typically linear, which indicates that for a given magnitude earthquake a larger number of earthquakes will occur of a lesser magnitude. For a slope of -1.0 , a ten-fold increase in the number of earthquakes will occur for a decrease in the magnitude of one.

The recurrence curve shown in Figure 5.6 is based on all of the natural earthquakes recorded at McCoy. A b-slope of -1.0 is shown for comparison. A b-slope of $-.9$ is considered an

RECURRENCE CURVE

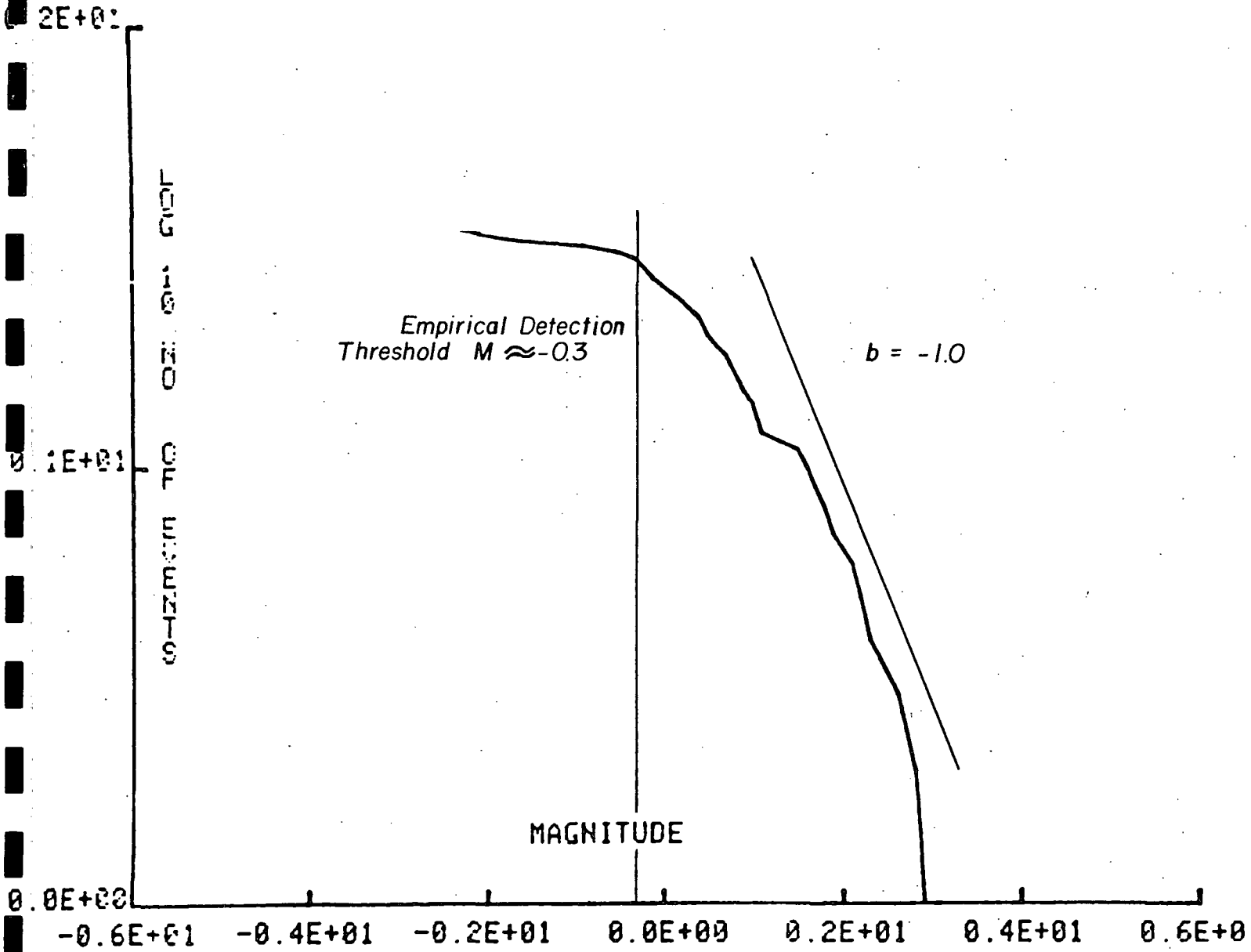


FIGURE 5.6

average value for world wide seismicity. The recurrence curve shown in Figure 5.6 is not smooth. The noise can be accounted for by the small number of earthquakes recorded.

As the magnitude decreases, the recurrence curve departs significantly from a straight line. This phenomenon is caused by the decreased capability of the seismograph array to detect these smaller earthquakes. An empirical detection threshold is determined to be the approximate point where the recurrence curve departs significantly from linearity at small magnitudes. This empirical detection threshold is shown in Figure 5.6. The empirical detection threshold is at approximately magnitude -0.4. This empirical detection threshold agrees closely with the detection threshold of -0.5 discussed in Section 5.2.1. Thus it can be surmised that all local earthquakes with magnitudes greater than -0.4 occurring during the survey have been detected.

5.2.5 Strain Release

The relationship between strain release and magnitude established by Richter is:

$$\text{Log}_{10} E = 9.4 + 2.14m - 0.054m^2$$

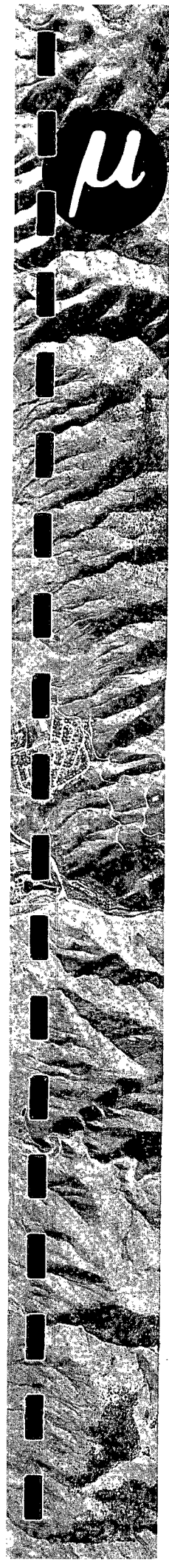
$$S = (E)^{\frac{1}{2}}$$

where

E is the energy released in ergs

S is the strain released in $(\text{ergs})^{\frac{1}{2}}$

m is the magnitude (Richter)



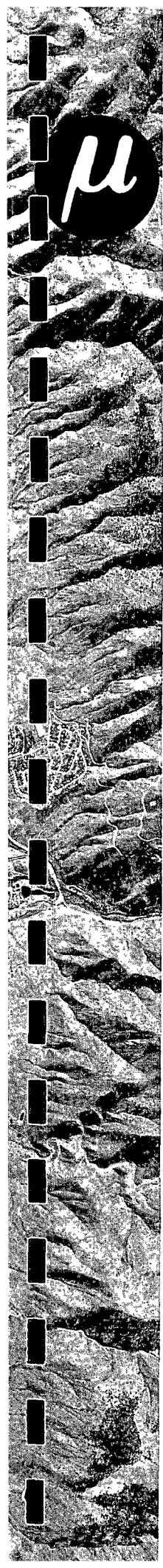
The purpose of estimating strain release is to get an idea of the total energy and total area of fracturing involved in the recorded earthquakes.

Plate 5.2 shows the strain release determined from both located and unlocated earthquakes. The unlocated strain release points are determined from S-P times at the stations at which the earthquake is detected. The strain release point is plotted at a point consistent with S-P times from two or more stations. For earthquakes detected on only one station, the strain release point is plotted at a point where the earthquake is most unlikely to have been detected by any other station.

The sparsity of earthquakes detected during the McCoy survey makes contouring of strain release difficult. Thus, in Plate 5.2, the solid parts of the contours indicate actual points of strain release. The dashed parts of the contours indicate possible epicenter and structural trends in the area.

5.2.6 First Motion Studies and Fault Plane Solutions

If seismographs record the direction of first motion of the P-phase arrival at several azimuths from the event, the double couple model of rock fracture will yield fault planes. A set of two orthogonal fault-plane solutions are determined; the preferred solution is denoted the fault-plane solution and the other the auxiliary solution. The first motion of the S-phase arrival can be used to choose between the two available solutions, but in practice, observation of first motions of the

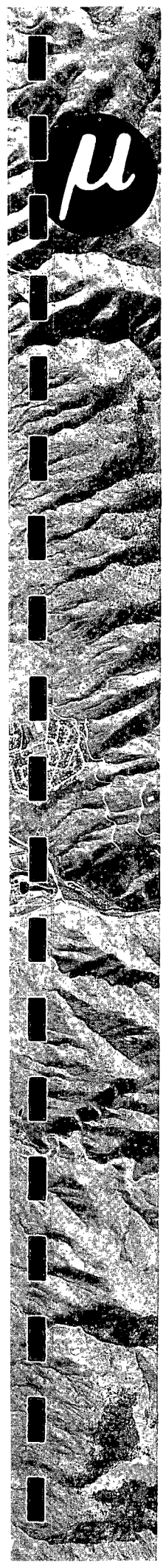


S-arrival is very difficult. In this case, hypocenter trends, mapped geologic structures, and general knowledge of tectonic stresses in the area are helpful in determining the preferred solution.

Fault plane solutions are shown in Plate 5.2. The first motion plots are upper hemisphere projections of the source emergence angle. The direction of first motion, dilatation (D) or compression (U), is plotted. Compressional quadrants are indicated by a vertically lined pattern. The fault plane solutions are poorly controlled due to poor azimuthal coverage for most of the located earthquakes. A majority of the fault planes determined show predominantly dip-slip motion along several possible fault plane orientations.

5.2.7 Poisson's Ratio

If the S-P times for a specific event are plotted versus the P-phase arrival times at several stations, the resultant points will fall on a straight line if the subsurface is homogeneous. The point where this line crosses the S-P = 0 axis corresponds to the origin time of the earthquake. If inhomogeneities in the subsurface are suspected, and an origin is available from the computer fit to the data, a straight line can be drawn between the computed origin-time and the point corresponding to each station. This line defines the average crustal properties along the line from the earthquake location to the station.



The crustal property defined is the P-wave to S-wave velocity ratio. The ratio is equal to the slope of the line plus 1.0. Such a plot is known as the Wadati plot (Figure 5.7). Individual-event Wadati plots are made for locatable events. It should be noted that the P-wave to S-wave velocity ratio acquired for each event is correct only along the raypath between the specific event and a particular station. The purpose of the composite is to give average values for the ratio under each station.

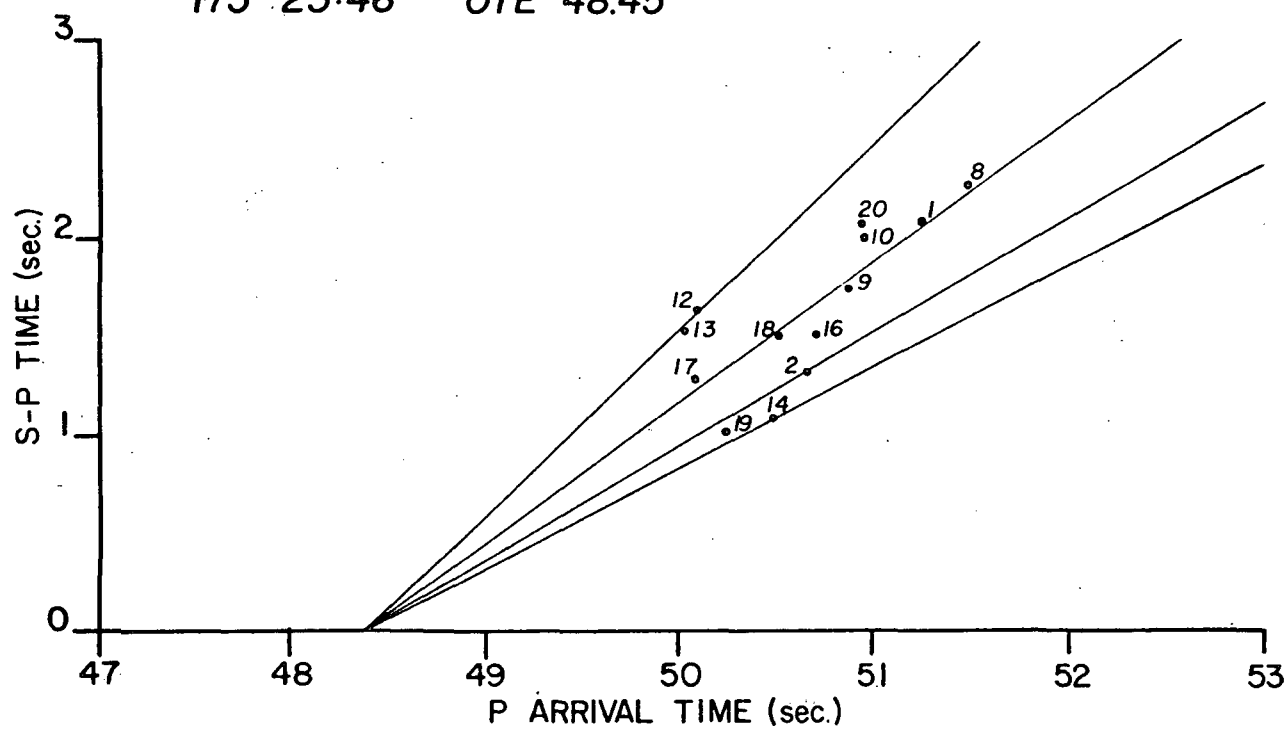
Another way of displaying the data is to convert the velocity ratio to Poisson's Ratio. The equivalent Poisson's Ratio for different slopes is also shown in Figure 5.7.

Once the Poisson's Ratio is determined for a specific raypath joining a station to an event location, the projection of the raypath on the surface is plotted on a map. The Poisson's Ratio map is shown in Plate 5.3.

Areas of high Poisson's Ratio (greater than .35) may indicate anomalously high fracture porosity. The areas of high Poisson's Ratio on Plate 5.3 include the boundaries of the seismograph array and the east central portion of the seismograph array near station 17. The high Poisson's Ratio in the boundary areas probably reflects the deep relatively unconsolidated sediments in the large basins surrounding the seismograph array. The high Poisson's Ratio near station 17 may indicate anomalously

WADATI DIAGRAM

175 23:46 OTE 48.45



176 02:24 OTE 36.70

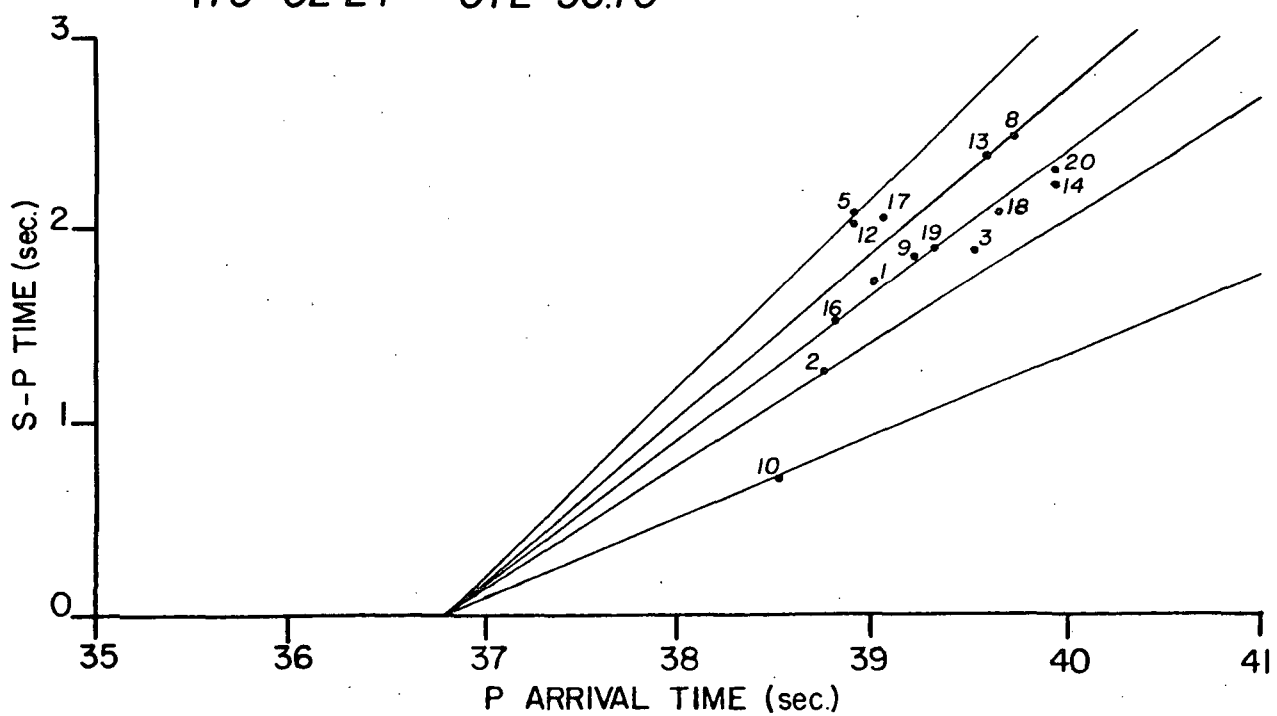
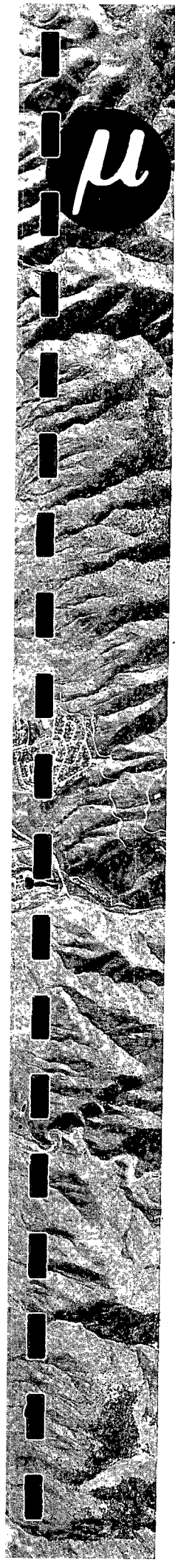


FIGURE 5.7

Drawn By: Teri Date: 10/1/79 Drawing No: McC-113 Checked By:



high fracture porosity or an anomalously high P-wave velocity in this area.

An area of low Poisson's Ratio (less than .15) is seen in the middle of the seismograph array. This area could indicate low fracturing or an area of anomalously low P-wave velocity or a combination of both. Poisson's Ratio will be discussed further in the interpretation section.

6.0.0 WAVE DELAY

6.1.0 Introduction

Separate phase arrivals from 9 teleseisms recorded during the McCoy survey are analyzed to provide information about deeper velocity structure in the survey area. Each arrival time is corrected to a datum 2.8 km below sea level. These corrections are based on the station elevations and the three dimensional velocity structure determined from the pseudo-refraction survey. Table 6.1 is a list of the teleseisms used for wave delay analysis.

6.2.0 Data Processing Methods

Arrivals from three phases of each teleseism are plotted on time-distance curves. The phase velocity of the teleseism is then drawn through each phase to produce the best fit to the measured arrival times. Figure 6.1 shows such a time-distance curve. Three phases are used to minimize the error in picking arrival times. Time residuals from the best fit to the phase velocity are averaged for each azimuth at which teleseisms approach the seismic array. The station showing the least variance from the best fitting phase velocity is used as a master station with a time residual of 0. Other time residuals are shifted to match the shift made to bring the master station to 0. In this survey station 5 shows the smallest time residuals and is assumed as the master station. Plate 6.1 shows the time residuals at each station relative to station 5.

TABLE 6.1
Teleseisms Recorded

Day	PDE Origin Time	Lat.°	Long.°	Depth (km)	Δ°	Phase Velocity (km/sec)	AZ°	INCL.°
173	6:30:56.3	17.05N	94.55W	112	31.5	12.62	S 51 E	27
175	1:11:33.4	23.65S	69.02W	100	81	20.94	S 51 E	16
176	5:29:07.5	5.13S	145.68E	195	98.5	24.34	S 86 W	14
176	11:01:12.1	20.06S	173.01W	33	79	20.35	S 53 W	16
177	3:49:21.4	22.30S	175.06W	33	82	21.26	S 48 W	16
178	8:50:39.1	70.10N	96.18W	33	32.5	12.69	N 12 E	27
178	9:50:08.7	7.17N	82.10W	33	46.5	14.21	S 57 E	24
179	14:44:00.0	37.14N	116.09W	0	3	8.10	S 28 E	45
181	8:33:04.0	7.11N	82.44W	33	46	14.20	S 57 E	24

All origin data is from the National Earthquake Information Center PDE printout for June-July, 1979.

All inclinations are taken from downward vertical.

ARRIVAL TIME VS. DISTANCE

178 09:58 S. Panama AZ=5 57°E V=14.21 km/sec Incl. = 24°

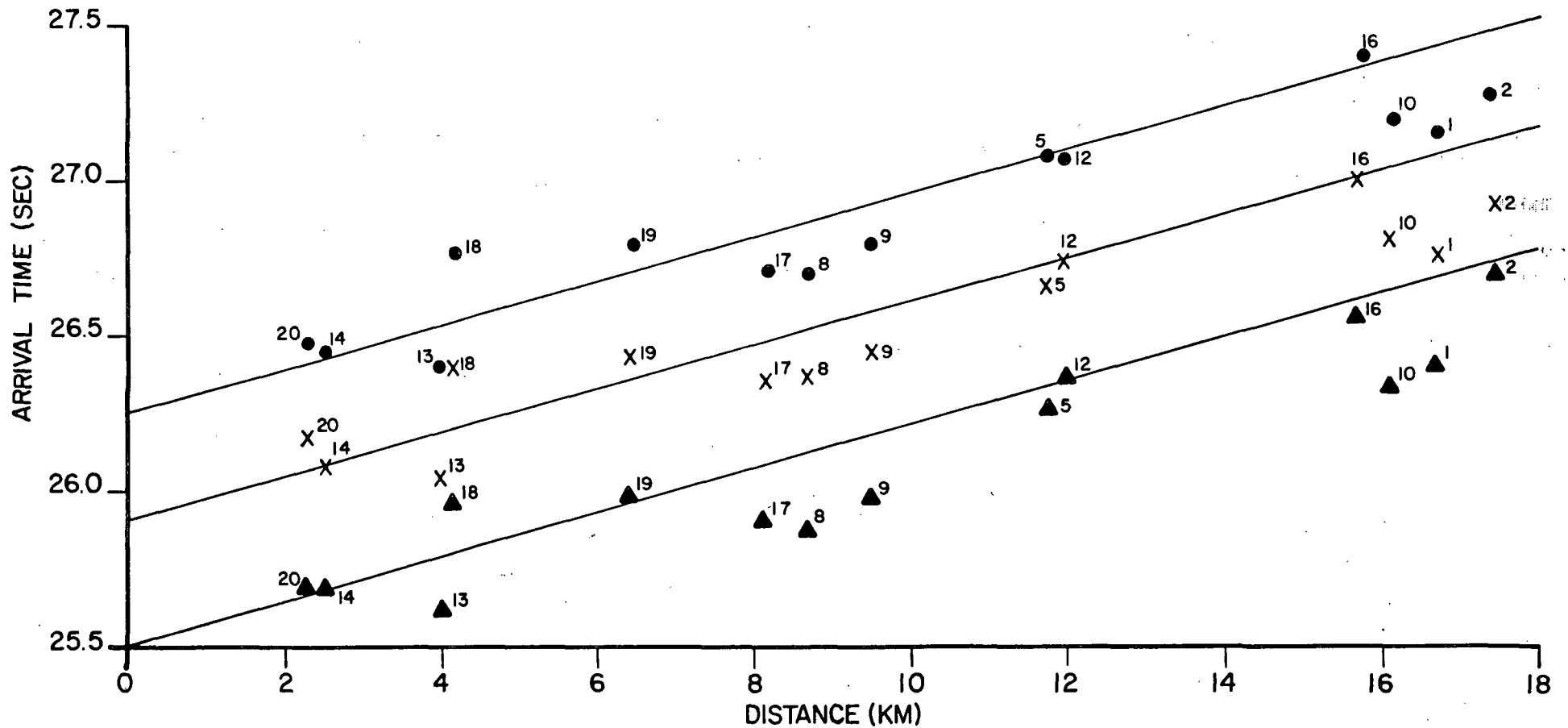
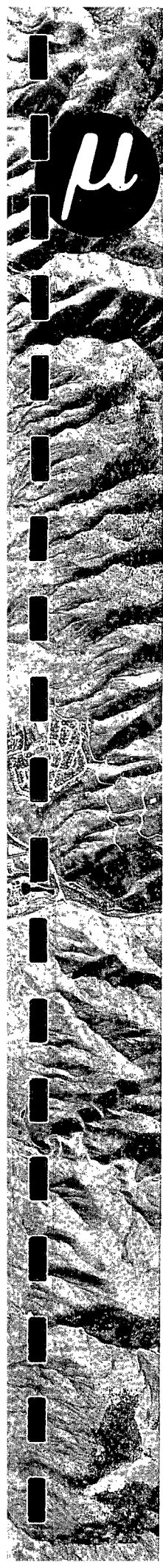


FIGURE 6.1



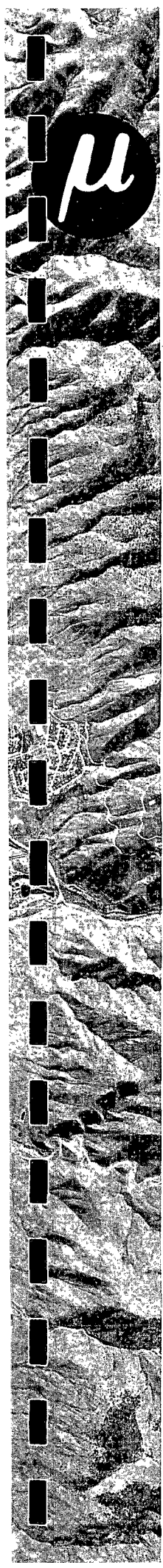
Time residuals are analyzed with a method analogous to the analysis of the pseudo-refraction residuals which is described in section 4.2. Advances and delays at different azimuths from each station can be accounted for by changes in the velocity structure under the station. However, unlike the pseudo-refraction analysis, there is no best fitting layered earth model to use as a basis for velocity changes under each station. The velocity changes can occur at any depth under the station. Therefore, a hypothetical wave delay surface is postulated. This surface is made to show an apparent velocity contrast of 10 km/sec. This apparent velocity contrast results in a 10 ms compensation for each 100 meters of replacement of material of one velocity with the other. The hypothetical wave delay surface used is the interface between two layers of:

5.75 km/sec from 4 km to 7 km

13.5 km/sec under 7 km

This hypothetical surface does not indicate actual velocity at a depth of 7 km. It is merely a convenient surface to show areas which have relative advances and delays.

One may then move the interface between these layers up or down at a rate of $(100\text{m}/10\text{ms} \times 1/\cos A)$ to account for travel time residuals. A is the emergence angle of the teleseism and $1/\cos A$ is the correction applied to the replacement rate for this emergence angle. The resulting depth to the 13.5 km/sec layer is plotted at the surface projection of the point at which the teleseism intersects the depth assigned for a station

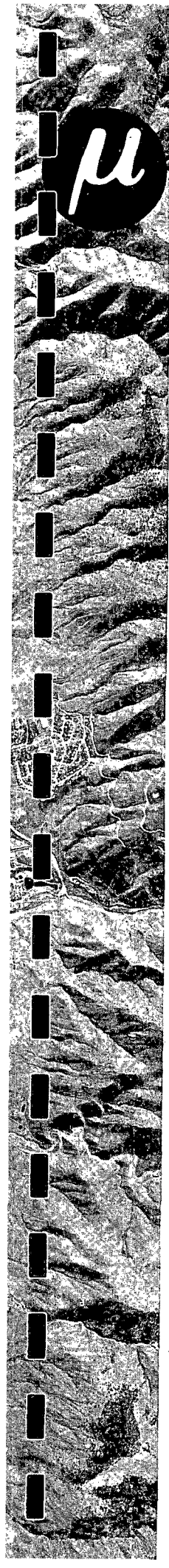


on the azimuth that the teleseism arrives. These points are contoured to show the wave delay surface. The wave delay surface is shown in Plate 6.2. The depths shown in Plate 6.2 do not indicate actual depths to structure. They show areas of relative advance and delay.

6.3.0 Observations

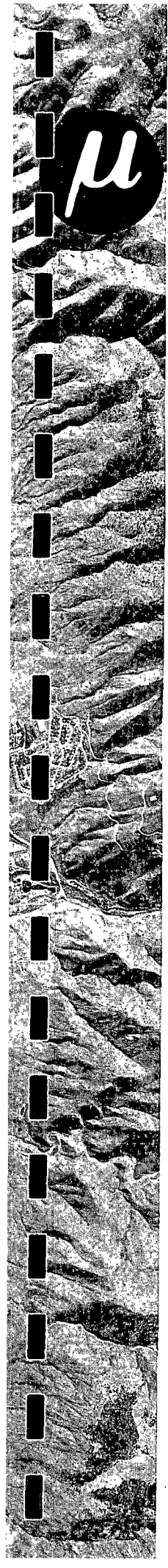
Relative advances and delays in the survey area are quite large. The difference between the largest advances and delays are on the order of 450 milliseconds. Areas showing the highest advances are indicated by the shallowest parts of the wave delay surface in Plate 6.2. The areas showing the wave delay surface shallower than 5.5 km are highlighted by a vertically lined pattern. Areas showing the highest delays are indicated by the deepest parts of the wave delay surface in Plate 6.2. The areas showing the wave delay surface deeper than 8 km are highlighted by a dotted pattern in Plate 6.2. It can be seen that the largest delays occur to the north, southwest and in the southeast section of the survey area. Wave delay observations are discussed further in the interpretation section.

7.0.0 COMPOSITE INTERPRETATION



Microearthquake activity during the McCoy survey was low. The activity was below one event per day. The most active area detected is southwest of the seismograph array, along the east side of Dixie Valley. The earthquakes located in Dixie Valley are quite large, ranging from magnitudes 1.9 to 3.1. Figure 4.2 shows that the active area in Dixie Valley is outside of the detection threshold distance for a magnitude 1.0 earthquake. Thus, these earthquakes may also be accompanied by smaller earthquakes which are too small to be detected at this distance. The area in which these Dixie Valley earthquakes occur agrees somewhat closely with the historical seismic activity in this area (see section 2.2.0).

The microearthquake locations inside the seismograph array agree quite well with the structure mapped using the pseudo-refraction technique. Fault plane solutions for these interior microearthquakes show predominantly dip-slip movement with small strike-slip components. This relative dislocation is consistent structure noted in the pseudo-refraction study. The faulting or dislocations occur along three orientations; north-northwest, west-northwest, and west-southwest. These orientations are significantly different from the predominantly north-east orientation of Basin and Range structure in general. This difference in orientation suggests a local rotation of the principal stress axes.



The area of high Poisson's Ratio shown near station 17 on Plate 5.3 coincides closely with the proposed faulting in the area of stations 7 and 17. This would indicate that the Poisson's Ratio high may be due to increased fracture porosity. The depth to the 5.0 km/sec refractor (Plate 4.1) is only about 2.5 km, so there may be considerable fracturing in the deeper rocks in this area. This is supported by the 7.8 km depth of the earthquakes located here.

The wave delay surface shown in Plate 6.2 has three areas which show significant delays. North and southwest of the survey area, these delays are poorly controlled by the pseudo-refraction survey. Thus the corrections made based on the pseudo-refraction velocity model may not reflect the actual near surface velocity structure at these fringes of the survey area. The area of large delay shown on Plate 6.2 in the southeast section of the survey area, however, is located where there is quite good control of the near surface velocity model from the pseudo-refraction survey. The large delays present (up to 200 ms) in this area suggest that there may be anomalously low velocity material underlying this area. Waves emerging from 14° to 45° all are delayed in this area. This would suggest that the low velocity material is somewhat near the surface.

Plate 7.1 is a composite interpretation map. Suspected active faults, areas of suspected increased fracture porosity, and the area suspected to have anomalously low velocity material underlying it are all shown on this map. Also shown are the structural highs from the pseudo-refraction survey.

8.0.0 SUMMARY OF CONCLUSIONS AND RECOMMENDATIONS

Conclusions and recommendations are necessarily based on data obtained during this survey and data available publicly. Revisions in the conclusions should be expected with any additional information.

8.1.0 Conclusions

8.1.1 The McCoy Prospect Area has a low rate of seismicity with an average of about 1 earthquake per day.

8.1.2 Earthquake magnitudes are low ($M < 1.5$) except in the Dixie Valley swarm ($1.9 < M < 3.1$).

8.1.3 Fault plane solutions indicate rotation of the principal stress axes locally.

8.1.4 The Poisson's Ratio high near station 17 suggests anomalously high fracture porosity in this vicinity.

8.1.5 Wave delay analysis indicates low velocity material underlying the southeast section of the seismograph array, in the vicinity of stations 18, 19, and 20.



MICROGEOPHYSICS SEISMOGRAPH SYSTEM INSTRUMENTATION

Introduction

The passive seismic system used for geothermal exploration and deployed by MicroGeophysics Corporation (MGC) is a hybrid system. The system consists of both independent seismographs and RF telemetered stations. The network station capability is from six to ten stations. A schematic of the system is shown in Figure 1. The independent stations are basically MEQ-800 visual drum recorders, with an integral timing system synchronized to universal coordinated time. As an option, the seismic signal can also be recorded by a continuous magnetic tape recorder. This independent station schematic is shown in Figure 1. The RF-telemetry system consists of from two to eight satellite stations with a central recording system. The satellite stations are comprised of a geophone, amplified voltage controlled oscillator with a RF transmitter.

The central system received data from each of the satellite stations, discriminates them, and records them. The recording can be on smoked paper, and/or magnetic tape, and/or event recording on a high speed photographic recording. A schematic is shown in Figure 1. A detailed explanation of each of the component parts for each system is given in the following sections.

L4-C Seismometer

The L4-C is a one-Hertz-natural-frequency vertical seismometer (manufactured by Mark Products). The damping is 0.6 of critical damping. The L4-C has an output of 6.9 volts per inch/second. A typical specification sheet is shown in Figure 2.

As sensor options, other geophones can be utilized. A common option is the L-10 geophone (manufactured by Mark Products). A typical specification sheet is also shown in Figure 2.

MEQ-800-B

The MEQ-800-B is a visual microearthquake recorder. The smoked drum recording has a nominal 120 mm/min rotation speed with a 1 mm spacing between succeeding traces. The stylus and trace width is 0.05 mm. The amplifier has a maximum of 120 db of gain and selectable corners at 1, 5, and 10 Hz. The high cut filter has selectable corners of 10, 20, and 75 Hz. The amplifier gains can be changed by precise 6 db steps down from 120 db. The maximum pen deflection is ± 25 mm and can be limited under severe ground noise conditions to ± 10 mm or ± 5 mm.

The integral timing system consists of a clock, whose drift rate is less than ± 1 part in 10^7 (approximately ± 10 ms per day) and can be set to standard time and adjusted at 16 ms increments. Time is displayed on each trace by a slight deflection of the pen each second.

SYSTEM SCHEMATIC

INDEPENDENT STATIONS

4-5 Stations Available
Remote Station Location

Components:

Geophone
↓
Amplifier
↓
Filters
↓
*Recorder
 Smoked Paper
 Digital Tape (optional)

TELEMETRY STATIONS

4-5 Stations Available
Remote Station Location

Components:

Geophone
↓
Amplifier
↓
Filter
↓
Voltage Controlled
Oscillator (VCO)
↓
RF Transmitter

CENTRAL STATION

Components:

RF Receiver

Discriminator

*Recorder
 Smoked Paper
 Event Detection
 Digital Tape

*Timing supplied by each station, synchronized daily.

FIGURE 1

L4-C SPECIFICATIONS

Open Circuit Damping (b_o) = 0.28 Critical

$$\text{Coil Current Damping } (b_c) = \frac{1.1 R_c}{R_c + R_s}$$

Total Damping (b_t) = $b_o + b_c$

L-4C 1.0 Hz GEOPHONE

Coil Resistance (ohms)	84	134	206	320	500	870	1280	2000	3500	5500
Transduction (volts/inch/sec.)	0.87	1.13	1.34	1.7	2.1	2.8	3.5	4.2	5.55	6.9
Transduction (volts/meter/sec.)	34.2	43.5	53	67	83	110	136	165	220	273
Coil Inductance (henries)	0.092	0.147	0.230	0.35	0.55	0.95	1.40	2.20	3.85	6.05
Analog Capacity (microfarads)	875	550	356	230	147	85	58	37	21	13.4
Analog Inductance (henries)	29	46.4	71	110	173	300	440	690	1200	1900
Shunt For 0.70 Critical Damping	133	215	333	520	810	1400	2070	3250	5650	8900
Shunt For 0.60 Critical Damping	205	325	500	780	1220	2120	3100	4900	8500	13400

L-10A SPECIFICATIONS

L-10A GEOPHONE

Suspended Mass (m) 12.5 grams

Open Circuit Damping (b_o) $b_o = \frac{4.2}{f} \pm 10\%$

Coil Circuit Damping (b_c) $b_c = \frac{15.7 \cdot R_c}{f(R_s + R_c)} \pm 10\%$

Analog Capacitance (C_c) $C_c = \frac{5010}{R_c}$

R_c = Coil Resistance C_c = Microfarads

Analog Inductance (L_m) $L_m = \frac{5.16 \cdot R_c}{f^2}$

f = geophone frequency L_m = henries

L-10B 4.5Hz

Coil Resistance (ohms)	21	34	54	90	138	215	374	590	940
Transduction (volts/inch/second)	0.193	0.245	0.30	0.387	0.49	0.60	0.80	0.98	1.25
Coil Inductance (henries)	0.004	0.006	0.010	0.016	0.024	0.038	0.067	0.105	0.167
Analog Capacitance (micro farads)	350	216	136	81.6	53.1	34.1	19.7	12.4	7.80
Analog Inductance (henries)	3.58	5.82	9.24	15.4	23.6	36.8	64.0	102	161
Shunt for 1.00 Critical Damping (ohms)	66.8	108.5	173	277	317	687	1200	1890	3000
Shunt for 0.70 Critical Damping (ohms)	191	311	494	824	1260	1750	3420	5410	8570
Shunt for 0.60 Critical Damping (ohms)	315	512	814	1355	2080	3240	5640	8910	10425

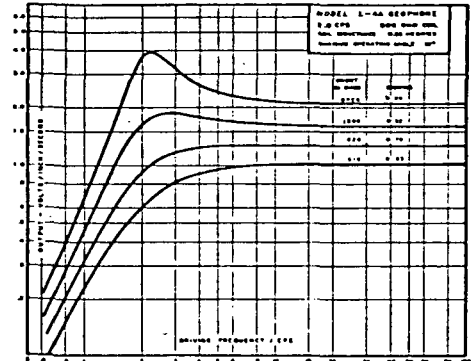
$b_o = .445$

$$b_c = \frac{2.33 R_c}{R_c + R_s}$$

FIGURE 2

L-4C 1.0 Hz GEOPHONE

- TYPE Moving dual coil, humbuck wound
- FREQUENCY 1.0 ± 0.05 Hz measured on 200 pound weight at 0.09 inches/second.
- FREQUENCY CHANGE WITH TILT Less than 0.05 Hz at 5° from vertical.
- FREQUENCY CHANGE WITH EXCITATION Less than 0.05 Hz from 0 to 0.09 inches/second
- SUSPENDED MASS 1000 grams
- STANDARD COIL RESISTANCES See Table
- LEAKAGE TO CASE 100 megohm minimum at 500 volts
- TRANSDUCTION POWER 8.8·10⁻³ watts inch second or 13.6 watts meter second
- OPEN CIRCUIT DAMPING (b_o) = 0.28 critical
- CURRENT DAMPING (b_c) = $\frac{1.1 R_c}{R_c + R_s}$
where: R_c = coil resistance - ohms
 R_s = shunt resistance - ohms
- COIL INDUCTANCE (L_c = 0.0011 R_c
 L_c in henries.
- ELECTRIC ANALOG OF CAPACITY $C_c = \frac{73,500}{R_c}$ (microfarads)
- ELECTRIC ANALOG OF INDUCTANCE $L_m = 0.345 R_c$ (henries)
- CASE HEIGHT 5 1/4 inches — 13 cm.
- CASE DIAMETER 3 inches — 7.6 cm.
- TOTAL DENSITY 3.7 grams cm³
- TOTAL WEIGHT 4 3/4 pounds — 2.15 kilograms
- OPERATING TEMPERATURE Range: -20 to 140° F or -29 to 60° C.
- OPERATING PRESSURE 500 PSI.



L-10B GEOPHONE

Suspended Mass (m) m = 19 grams

Open Circuit Damping (b_o) $b_o = \frac{2}{f} \pm 10\%$

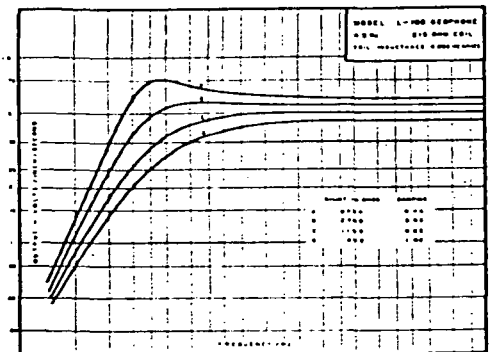
Coil Circuit Damping (b_c) $b_c = \frac{10.5 \cdot R_c}{f(R_s + R_c)} \pm 10\%$

Analog Capacitance (C_c) $C_c = \frac{7330}{R_c}$

R_c = Coil Resistance C_c = Microfarads

Analog Inductance (L_m) $L_m = \frac{3.41 \cdot R_c}{f^2}$

f = geophone frequency L_m = henries



INSTRUMENT RESPONSE

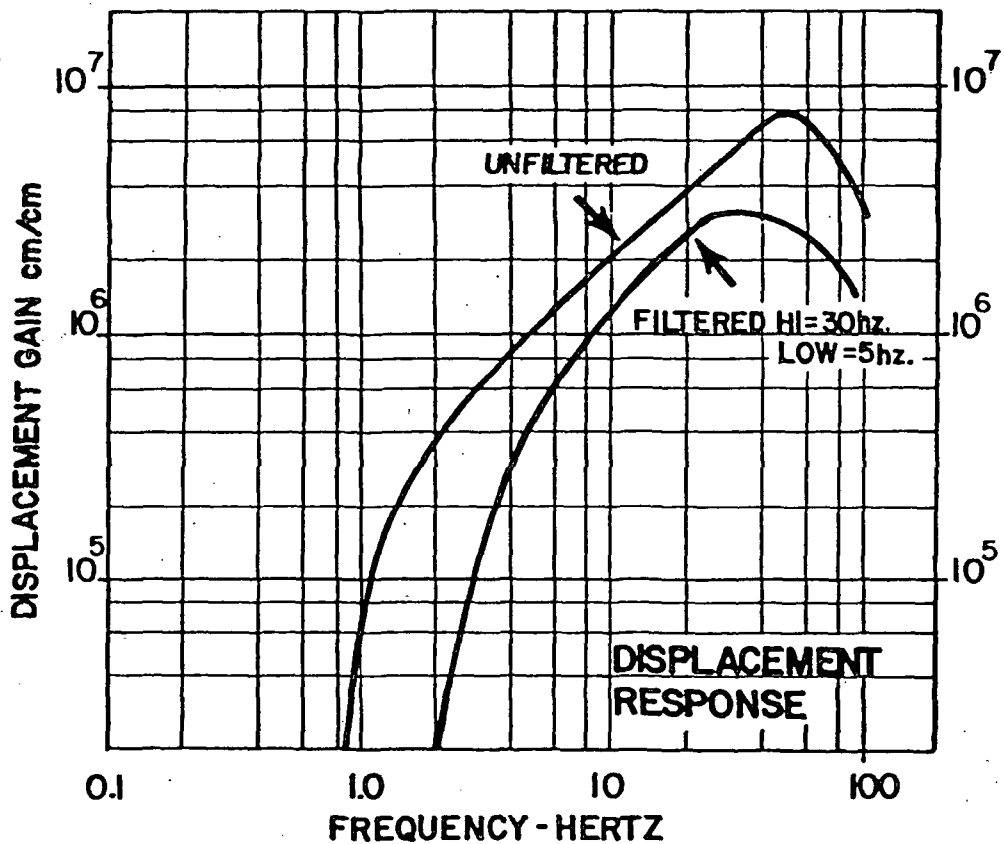
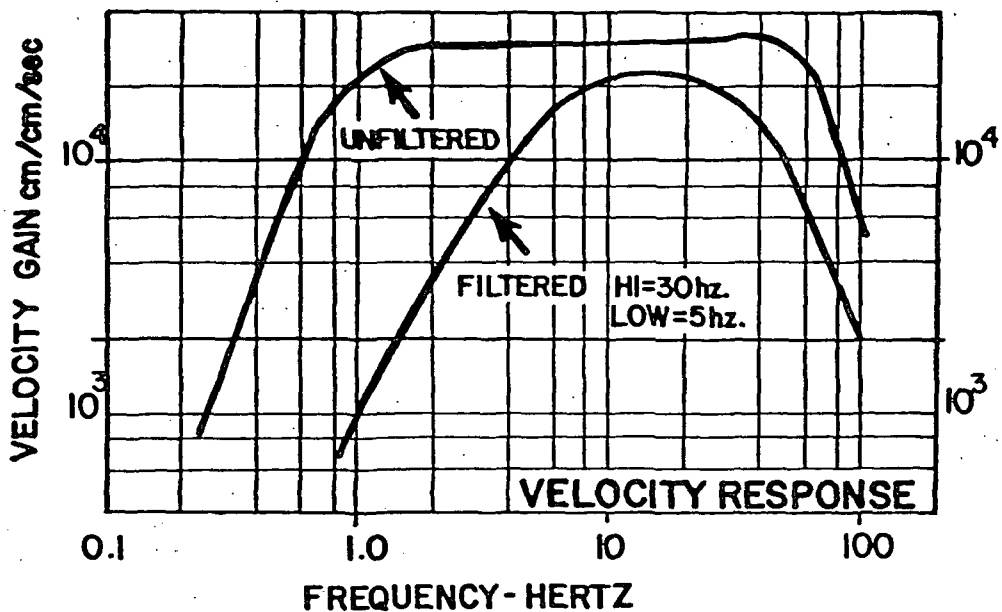


FIGURE 3

The frequency characteristics of the instrument with an L4-C are summarized in Figure 3. Both the velocity and displacement response for the MEQ-800-B microearthquake system are shown. The displacement response at a particular frequency (f) can be calculated by multiplying the velocity gain at f time $2\pi f$. The filter response and gain level shown are typical settings for operations in the western continental United States.

DMTR

The digital magnetic tape recorder (DMTR) is a twelve-bit 100 sampler-per-second, reel-to-reel-recorder which records data continuously. Each data block begins on the minute at the command of the clock in the MEQ-800-B system. The hour and minute from the clock are written at the beginning of each block. WWVB is recorded continuously on one bit of the tape format. The dynamic range of 72 db on this tape recorder allows the recovery of data under exceptionally noisy conditions.

WWVB

WWVB is the radio call code for the National Bureau of Standards 60 kHz time-standard station in Fort Collins, Colorado. The WWVB time standard is used to set and synchronize the micro-earthquake system clocks. As shown in Figure 4 below, the signal consists of 60 markers each one minute, with one marker each second (time progresses from left to right). Each marker is generated by reducing the power of the carrier by 10 db at the beginning of the corresponding second and restoring it:

- (1) 0.2 seconds later for a binary zero
- (2) 0.5 seconds later for a binary one
- (3) 0.8 seconds later for a 10 second position marker and for a minute reference marker

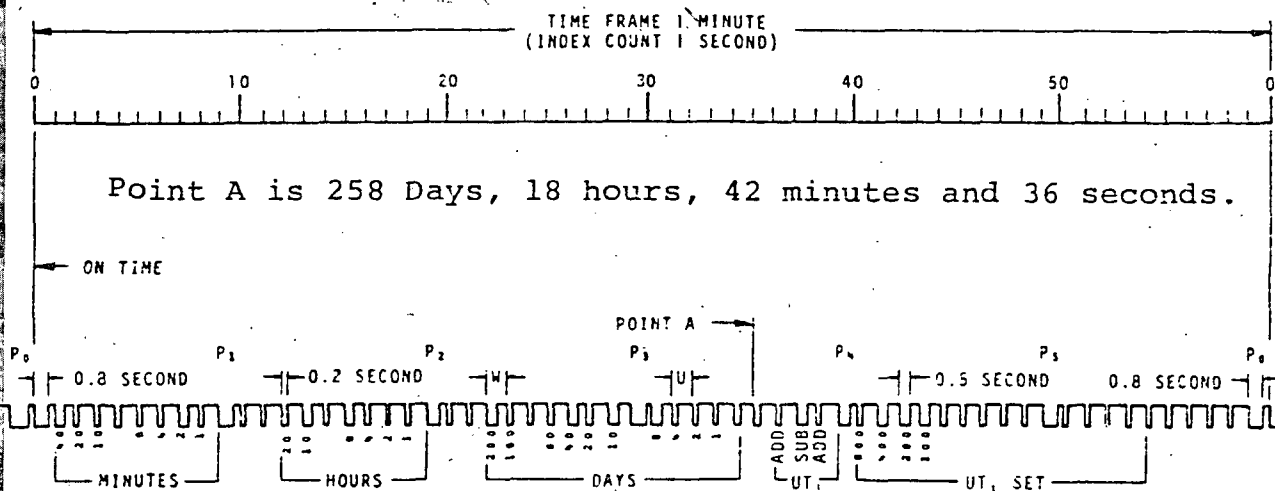
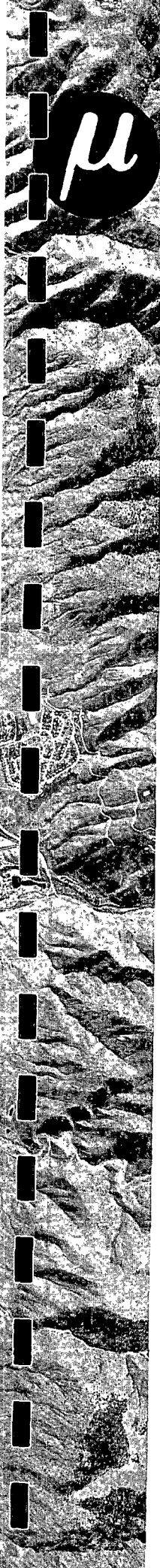


FIGURE 4



The WWVB code (as shown in Figure 3) is recorded daily on the visual drum as absolute time and date identification of the record, and is used to synchronize each MEQ system to standard time.

The MEQ systems' clocks are synchronized daily with WWVB by comparing (on an oscilloscope) the beginning of the WWVB second pulse with the MEQ-800-B internally generated one-second pulse. This comparison can be done to ± 2 milliseconds. Daily records are kept on the amount of correction for each clock. These time corrections are then applied to the records. Common corrections are on the order of 15 ms per day or less than one millisecond per hour.

WWV

WWV is the radio call code for the National Bureau of Standards 5, 10, 15, 25 MHz time standard station in Fort Collins, Colorado, as used by MicroGeophysics Corporation. The voice channel is used to generally coordinate time, while the second signals are used to precisely coordinate time. The use is similar to that of the WWVB channel.

Amplifier

The amplifier used is the AS-110 (manufactured by Sprengnether Instrument Company). This amplifier has identical characteristics to the Sprengnether MEQ-800 amplifier.

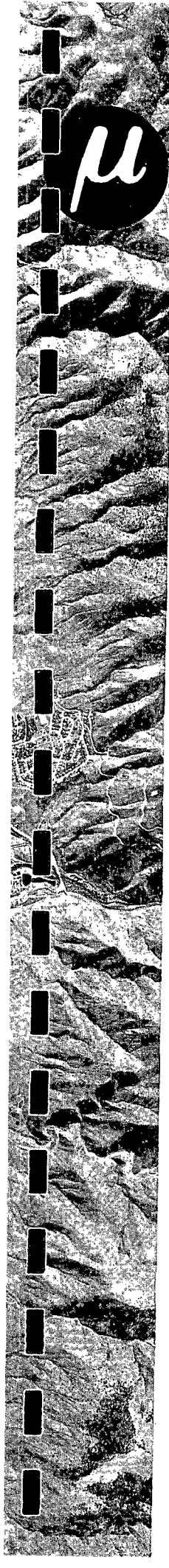
Telemetry

The following are excerpts for the Sprengnether Manual for the VCO and Discriminator equipment:

Telemetry VCO TC-10

The TC-10 Voltage Controlled Oscillator has been designed to fill a need for low cost, low power, high quality and versatile audio frequency telemetry components. Available in standard constant bandwidth channels from 340 to 3060 Hz with ± 125 Hz deviation the TC-10 VCO satisfies requirements for FM geophysical data telemetry in the frequency range DC to 50 Hz by telephone, land line, or by radio link. When used with the companion TC-20 Discriminator, 60 dB dynamic range (peak measurement is achieved in the 0-10 Hz bandwidth.

Versatility and simplicity of installation are assured by several special features incorporated into the VCO that are not normally available at such low cost. Eleven sensitivity ranges, from



50 mv to 100 v full scale deviation, are selectable on the front panel to facilitate system gain adjustments or multi-gain operations. Upper and lower band edge deviations can be effected from a front panel switch for ease in system setup and servicing. Center frequency, deviation, and output level can be monitored and adjusted from the front panel. Output is transformer coupled for flexible installation.

Power requirements are generous at ± 10 to 15 VDC at 15 ma for low power remote field installations. Small physical size is ideal for compact field case installation (the TC-10 matches the AS-110 amplifier in size and connector configuration) or for high density packing in rack mount multi-channel operations.

The TC-110 VCO represents state-of-the-art in circuit design, user convenience, and low price, satisfying virtually all requirements for high quality audio frequency FM telemetry.

Discriminator TC-20

The TC-20 Discriminator has been designed to fill a need for low cost, low power, high quality and versatile audio frequency telemetry components. Available in standard constant bandwidth channels from 340 to 3060 Hz with ± 125 Hz deviation the TC-20 satisfies requirements for FM telemetry of geophysical data in the frequency range DC to 50 Hz by telephone or land line or by radio link. When used with the companion TC-10 VCO, 60 dB dynamic range (peak measurement) is achieved in the 0-10 Hz bandwidth.

Several unique features are found on this low cost phase-locked loop discriminator that normally are incorporated only in more expensive units. A sense light on the front panel indicates low carrier level. Provision is made for a reference compensation tone and trim to effect compensation for frequency shifts in multiplexed tone bundles. The TC-20 also provides for an auxiliary-test input on the front panel to facilitate service checks and adjustments. The carrier after filtering can be monitored from the front panel and all major adjustments are made with front panel controls. The input is transformer coupled for flexibility in installation.

Power requirements are ± 10 to 15 VDC at 18 ma. Output filters (3 pole Butterworth) at 1, 5, 10, 20, 50 Hz (3dB) are available, factory adjusted. The panel width of 1-1/2" allows dense packing in rack installations.

The TC-20 represents state-of-the-art in phase-locked loop discriminators, offering the maximum in flexibility and convenience features at the lowest possible cost.

RF Telemetry Link

These RF telemetry links are Monitron low-power FR transmitters and receivers (manufactured by Monitron Corporation). The output power is less than 100 mw. Specifications are shown below.

System Gains: The typical gains of each system with typical settings are shown below:

System: MEQ-800 (Smoked Paper)

Filter Settings:

Hi = 30 Hz

Lo = 5 Hz

Geophone L4-C

Gain Settings

Displacement Gain at 20 Hz

60	0.04	x	10^6
66	0.08	x	10^6
72	0.16	x	10^6
78	0.33	x	10^6
84	0.65	x	10^6
90	1.3	x	10^6
96	2.6	x	10^6
102	5.2	x	10^6

System: VCO-TELEMETRY-VR-60

Filter Settings

Hi = 30 Hz

Lo = 5 Hz

Geophone L4-C

VCO = 5 Volts/f.s.

VR-60 + 100 mv/mm

Gains Settings

Displacement Gain at 20 Hz

60	0.2	x	10^6
66	0.4	x	10^6
72	0.8	x	10^6
78	1.65	x	10^6
84	3.25	x	10^6
90	6.5	x	10^6
96	13.0	x	10^6
102	26.0	x	10^6

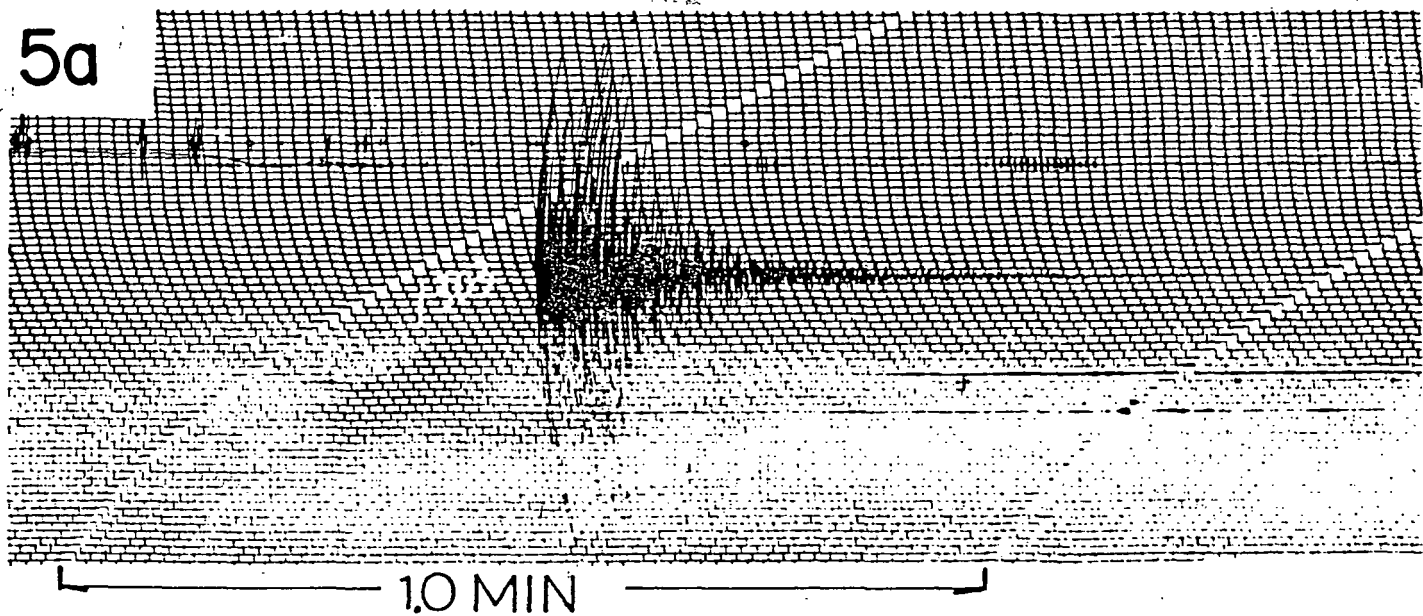


DATA

An example of the output of a microearthquake system is shown in Figure 5. The smoked-paper output is shown in Figure 5(a) while Figure 5(b) and Figure 5(c) are the same earthquake recorded on magnetic tape and played back at two different speeds. The playback format is illustrated in the figure.

The smoked-paper record is used at the time of the recording (in the field) to estimate the seismicity and to locate any recorded microearthquake approximately. The paper records can be picked under magnification to a precision of less than ± 30 ms. The magnetic tape playbacks are then used to increase the timing precision of an event to ± 10 ms., a precision close to the subjective level of interpretation by an experienced seismologist. The magnetic tape playbacks are also useful in increasing the effective gain of recording and thereby recording very small amplitude events. In noisy areas, the tape playbacks can be used to recover data obscured on the paper monitor records by cultural noise on adjacent traces.

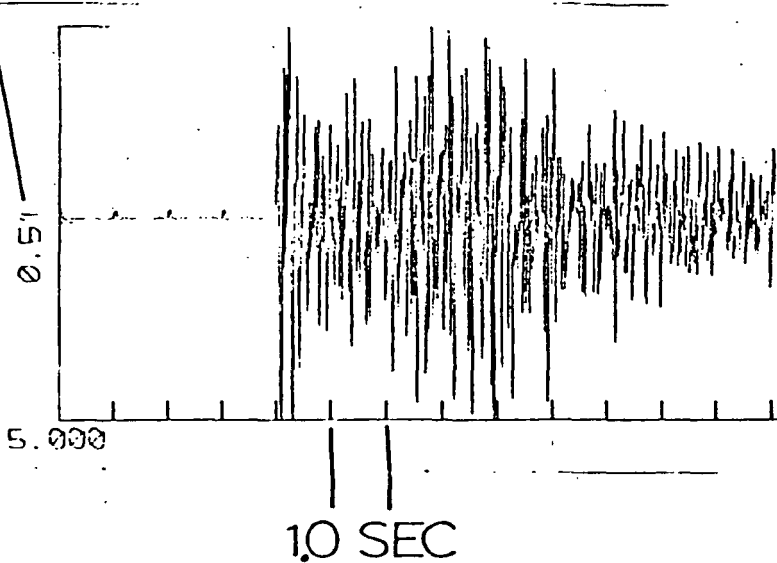
5a



5b

Plot gain in db above station gain

STATION NUMBER — 3
 GAIN IN db — 90
 TIME (DAY, HOUR, MIN) — 159 13 3
 STARTING SEC — 5.000
 DRUM SPEED (MM/SEC) — DRNSPD: 7.00

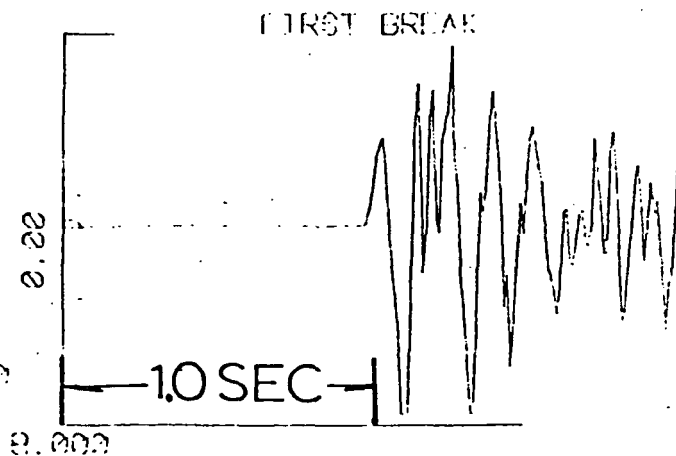



5c

NI424.R04

3
 90
 159 13 3
 5.000

DRNSPD: 40.00






Microearthquakes

The correlation of microearthquakes and commercial geothermal reservoirs is empirical. However, a high rate of seismicity is a sufficient ingredient in several geothermal system models. One such model is based on the probable chemistry within a convecting system. As hot water or steam rises closer to the surface, it cools slightly and precipitates considerable material. Without the production of fresh conduits, the system will be plugged and the efficient convection mechanism will be terminated. Another model simply requires a fractured medium for deep convective circulation of meteoric waters to depths at which the normal gradient will produce commercially useful temperatures. In the second model, contemporary fracturing is not necessary. However, the best evidence for the existence of fractures may be present seismic activity.

Almost all sets of earthquakes for which magnitudes have been measured, follow an inverse straight-line relationship between the log of the number of earthquakes and magnitude. In general, a decrease in magnitude by 1.0 is accompanied by an increase in a factor of 10 or more in the number of events occurring. Thus, if the detection capability can be increased by one magnitude, 10 or more events will be recorded for every one previously recorded. To do this, a prospect area is blanketed with seismic stations at a nominal station spacing of 4-6 km. These stations, recording the ground motion at displacement gains of $1-3 \times 10^6$ at 20 Hz, will record seismic arrivals of earthquakes down to Richter magnitude zero or below. Timing resolutions between stations is held to less than a few milliseconds and time differences of the arrivals for any pair of stations is determined.

In order to locate an event in space, a velocity distribution must either be assumed or determined. Most velocity models are one dimensional with the velocity varying between constant velocity layers. Other models allow the velocity to increase linearly with depth or with vertical travel time. Ignorance of the exact velocity model causes an accuracy problem in the computed locations. However, precision is affected little by the velocity model.

Microearthquake signals are dominated by frequencies between 5 to 25 Hz, making the picking of the onset somewhat subjective at the ± 5 ms level independent of the playback speed. This type of error causes the location to lose precision. This error can be controlled by a trained seismologist whose picks will be consistent.



The size of the expected location error is not easily addressed. The problem is complicated by geometry, velocity models, and geology. However, for an event recorded on eight or more stations with a nominal station spacing 5 km and minimum timing and velocity errors, the location should be precise to within $\pm\frac{1}{2}$ km in plan and ± 1 in depth. Errors in the computed location will increase outside the network of stations.

Once the event locations are finalized, their relationships with possible geology or active faulting can be made. The statistics of occurrence can also be used to characterize an area. A list of products from a microearthquake survey follows:

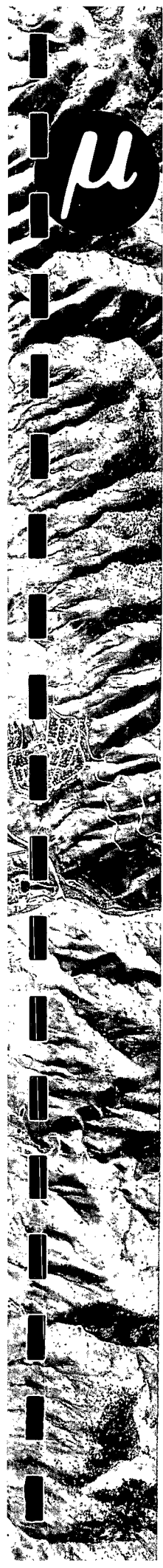
- Hypocenter Map
- Fault Plane Solutions
- Occurrence Statistics
 - Event list
 - Recurrence curve
 - Clustering statistics (swarming)
- Rock Properties Distribution
 - Velocity distribution
 - Poisson's Ratio distribution


An interpretation of the above results in terms of active fault identification and modes of deformation, identification of volumes of rock with anomalous properties, seismic safety, and recommendations.



MICROEARTHQUAKES BIBLIOGRAPHY

- Aki, Keiiti, A note on the use of microseisms in determining the shallow structures of the earth's crust (Random waves correlation earth): *Geophysics*, v. 30, no. 4, p. 665.
- Brune, J.N., and Allen, C.R., 1976, A microearthquake survey of the San Andreas fault system in Southern California: *Bull. Seismol. Soc. Am.*, v. 57, no. 2, p. 277-296.
- Caton, P.W., 1976, Plane wave apparent velocity vector techniques for evaluating and improving location accuracies with data obtained from small arrays (7 to 10 km in diameter): Unpublished paper, 71 p.
- Cheatum, C., and Combs, J., 1973, Microearthquake study of the San Jacinto Valley, Riverside County California: from the Proceedings of the Conference on Tectonic Problems of the San Andreas Fault System, p. 1-10.
- Combs, J., and Hadley, D., 1977, Microearthquake investigation of the Mesa geothermal anomaly, Imperial Valley, California: *Geophysics*, v. 42, p. 17-33.
- _____, and Robstein, Y., 1976, Microearthquake studies in the Coso geothermal area, China Lake, California: *Proc., 2nd U.N. Sympos. Develop. and Use of Geothermal Resources*, v. 2, p. 909-916.
- Crosson, R.S., 1972, Small earthquakes, structure and tectonics of the Puget Sound region: *Bull. Seismol. Soc. Am.*, v. 62, p. 1133-1171.
- Dahl, A.H., and Johnson, B.D., 1974, Preliminary results of a microseism study for the region around the Snake River Plain (1973-March 1974): Preprint presented at the Idaho Academy of Sciences, Ricks College, Rexburg, Idaho, April 19-20, 1974.
- Douglas, B.M., and Ryall, A., 1972, Spectral characteristics and stress drop for microearthquakes near Fairview Peak, Nevada: *Jour., Geophys. Res.*, v. 77, p. 351-359 .
- Fitch, T., 1969, Microearthquake activity following the Parkfield, California earthquake of June 1966: *Bull. Seismol. Soc. Am.*, v. 59, no. 2, p. 603.
- Hadley, D., and Combs, J., 1974, Microearthquake distribution and mechanisms of faulting in the Fontana San Bernadino area of Southern California: *Bull. Seismol. Soc. Am.*, v. 64, p. 1477-1499.

- 
- Hamilton, R.M., and Muffler, L.J.P., 1972, Microearthquakes at the Geysers geothermal area, California: Jour. Geophys. Research, v. 77, no. 11, p. 2081-2086.
- Johnson, L.A. and Butler, D., 1975, Prediction analysis applied to microearthquake hypocenter location: abstract in Abstract and Biographies of the 45th Annual International Meeting of the Society of Exploration Geophysicists, Tulsa, Oklahoma, paper GT-15.
- Kisslinger, C., and Engdahl, E.R., 1974, Semyenov Prediction, Test of the Semyenov Prediction Technique in the Central Aleutian Islands: Tectonophysics, v. 23, p. 237-246.
- Knapp, R.B., and Knight, J.E., 1977, Differential thermal expansion of pore fluids: Fracture propagation and microearthquake production in hot pluton environments: Jour. Geophys. Research, v. 82, p. 2515-2522.
- Lange, A.L., and Westphal, W.H., 1969, Microearthquakes near the Geysers, Sonoma County, California: Jour. Geophys. Research, v. 74, p. 4377-4378.
- Langenkamp, D., and Combs, J., 1974, Microearthquake study of the Elsinore Fault Zone, Southern California: Bull. Seismol. Soc. Am., v. 64, p. 187-203.
- Leslie, H.D., et al, 1976, Microearthquake location using a maximum likelihood processor: Geophysics, v. 41, no. 5, p. 960-969.
- Liaw, A.L., 1977, Microseisms in geothermal exploration; studies in Grass Valley, Nevada: PhD Thesis, University of California, Berkeley, California.
- Michaels, P.J., 1973, An application of the generalized linear inverse method in the location of microearthquakes and simultaneous velocity model determinations: MS Thesis, University of Utah, Salt Lake City, Utah.
- Oliver, J.E., 1966, Microearthquakes: ESSA Sympos. on earthquake prediction, Rockville, Maryland, Feb. 7-9, 1966, U.S. Dept. of Commerce, Environmental Sciences Services Admin.
- Pennington, W.D., Smith, R.B., and Trimble, A.B., 1974, A microearthquake survey of parts of the Snake River Plain and Central Idaho: Bull. Seismol. Soc. Am., v. 64, no. 2, p. 307-312.
- Peters, D.C., and Crosson, R.S., 1973, Application of prediction analysis to hypocenter determination using a local array: Bull. Seismol. Soc. Am., v. 62, no. 3, p. 775-788.



Sanford, A.R., et al, 1976, Microearthquake investigations of magma bodies in the vicinity of Socorro, New Mexico: Geological Society of America, 1976 Annual Meeting, Denver. Abstracts: p. 1085-1086.

_____, Alptekin, O., and Topozada, T.R., 1973, Use of reflection phases on microearthquake seismograms to map an unusual discontinuity beneath the Rio Grande Rift: Bull. Seismol. Soc. Am., v. 63, p. 2021-2034.

_____, Carapetian, A.G., and Long, L.T., 1968, High frequency microseisms from a known source: Bull. Seismol. Soc. Am., v. 58, no. 2, p. 639-644.

_____, and Singh, S., 1968, Microearthquake activity, minimum recording time for determining short-term seismicity forms: Bull. Seismol. Soc. Am., v. 58, no. 2, p. 639-944.

Spinel, R.C., et al, 1974, Microearthquake survey of median valley of the Mid-Atlantic Ridge at 360°30"N: Nature, v. 248, p. 577-579.

Steeple, D.W., and Pitt, A.M., 1976, Microearthquakes in and near Long Valley, California: Jour. Geophys. Research, v. 81, no. 5.

Ward, P.L., 1972, Microearthquakes: prospecting tool and possible hazard in the development of geothermal resources: Geothermics, v. 1, no. 1, p. 3-12.

_____, and Bjornsson, S., 1971, Microearthquakes, swarms, and the geothermal areas of Iceland: Jour. Geophys. Research, v. 76, no. 17, p. 3953-3982.

_____, and Jacob, R.H., 1971, Microearthquakes: In the Ahuachapan geothermal field, El Salvador, Central America: Science, v. 173, p. 328.

_____, Palmason, G., and Drake, C., 1969, A microearthquake survey and the Mid-Atlantic Ridge in Iceland: Jour. Geophys. Research, v. 74, p. 665-684.